Misalignment algorithm of a wide-field survey telescope based on third-order quadratic nodal aberration theory

Jinxin Wang,[a,b] **Xu He**,[a,b,*] **Xiaohui Zhang**,[a] and **Jing Luo**[a]
[a]Chinese Academy of Science, Changchun Institute of Optics, Fine Mechanics and Physics, Changchun, China
[b]University of Chinese Academy of Sciences, Beijing, China

Abstract. Off-axis three-mirror anastigmatic (TMA) telescopes with designed decenters and tilts, have many misalignment degrees of freedom and strong coupling between each misalignment degree of freedom. Therefore, it is difficult to establish misalignment equations only using A222 and A131 in nodal aberration theory (NAT). In addition, for off-axis TMA optical systems with designed decenters and tilts, the robustness of the existing fifth-order NAT misalignment calculation algorithm based on high-order Zernike coefficients and boresight errors decreases, so it is difficult to realize its engineering application. To solve the issue of insufficient practicality of the existing misalignment algorithm based on fifth-order NAT, a third-order NAT calculation algorithm based on quadratic aberration field decenter vectors is derived and established. Two concepts of inherent aberration field decenter vector and misalignment aberration field decenter vector are proposed. Taking an off-axis TMA optical system with 6-m focal length as the research object, simulations, and alignment verification experiments were carried out. Compared with the existing fifth-order NAT misalignment algorithm, the results show that when measurement noise is not considered, the two methods can both obtain convergent calculation results, and the average RMS wavefront errors (WFE) of the optical system are both corrected to be below 0.0574 waves. When different levels of measurement noise are introduced, the robustness of the fifth-order NAT misalignment algorithm decreases, and there are even cases where the optical system completely fails to be corrected. However, the algorithm based on quadratic aberration field decenter vectors shows better robustness. Under different levels of measurement noise, this algorithm could correct the average RMS WFE of the optical system to around 0.0574 waves. © *2021 Society of Photo-Optical Instrumentation Engineers (SPIE)* [DOI: 10.1117/1.JATIS.7.4.049003]

Keywords: aberration field decenter vector; alignment; misalignment; robustness; nodal aberration theory; off-axis three-mirror anastigmatic telescope.

Paper 21039 received Mar. 31, 2021; accepted for publication Oct. 14, 2021; published online Nov. 6, 2021.

1 Introduction

As the size of aperture and field of view (FOV) increase, the resolution, breadth, and depth of observation of space astronomical telescopes have been gradually raised.[1,2] To ensure the accuracy of astronomical observation data in a wider FOV, it is necessary for wide-field telescopes to have high imaging quality in both meridian and sagittal direction.[3–6] However, it is difficult for the existing three-mirror anastigmatic (TMA) optical path to take both of them into account. Therefore, an off-axis TMA system with designed decenters and tilts is proposed.[7] Conventional off-axis reflection optical systems are difficult to effectively balance the aberrations of off-axis FOV in meridian direction,[1,8] whereas the introduction of tilts and decenters in the design process of the optical systems can effectively balance the aberrations of off-axis FOV in the two dimensions of meridian and sagittal, which can effectively improve the image quality. The off-axis TMA systems with designed decenters and tilts, is currently an important type of

*Address all correspondence to Xu He, hexu_ciomp@sina.com

2329-4124/2021/$28.00 © 2021 SPIE

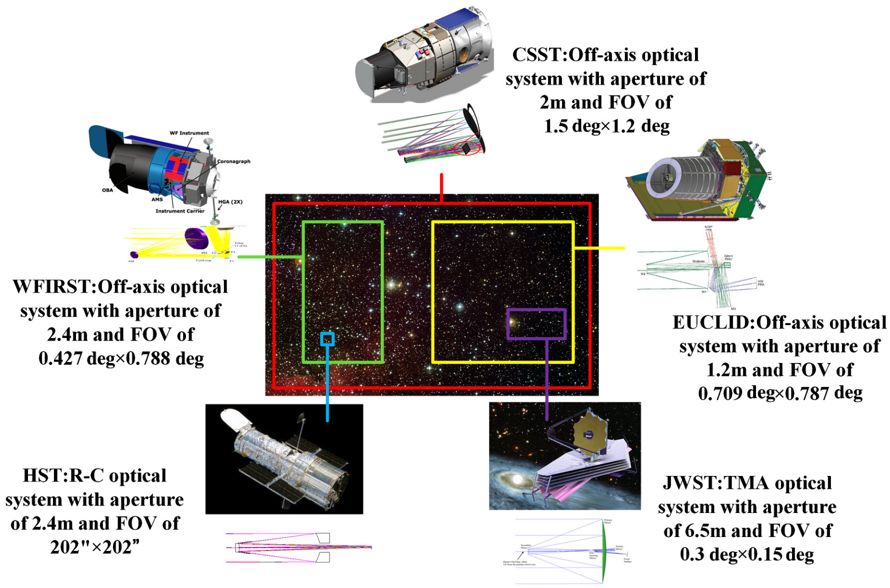

Fig. 1 Space astronomical telescopes with large aperture and wide FOV.

non-rotationally symmetrical structure used in the research and design of space astronomical telescopes with wide FOV and large aperture.[1,8] As shown in Fig. 1, tilts and decenters have been introduced into the optical path of the Wide-Field Infrared Survey Telescope (WFIRST) that is currently under development in the United States, the Spectral Survey Telescope of the European Space Agency (EUCLID), and the China Space Station Project Survey Telescope (CSST) that is now under demonstration in China, to enlarge the systems' effective FOV and improve the resolution of them. Compared with Hubble Space Telescope (HST) and James Webb Space Telescope (JWST), the observation breadth of these new space telescopes has been greatly improved.[9,10]

With tilts and decenters introduced into an off-axis reflective optical system, it could also be referred to as a non-rotationally symmetric system because it has no definite axis of symmetry.[7] This makes it difficult for traditional "compensation alignment methods" to make each optical surface coincide with the design position during the ground alignment of space telescopes,[11] and the initial alignment accuracy is low. A large initial alignment error will affect the key performance of space telescopes, such as PSF and optics ellipticity.[12] Computer-aided alignment (CAA) technology has unique advantages in fine alignment of space telescopes. However, the existing numerical misalignment calculation algorithms, such as sensitivity matrix and inverse optimization algorithm, have limitations. For wide-field and large-aperture off-axis TMA systems, with large initial alignment error threshold and large Zernike coefficient measures noise, the results calculated using the numerical misalignment calculation algorithms is difficult to converge.[11,13,14]

Analytical algorithms based on nodal aberration theory (NAT) are dedicated to studying the complex functional relationship between misalignments and aberrations of optical systems. This creates an opportunity to solve the limitations of numerical algorithms.[15–17] NAT was first established by Shack[18] and later improved by Thompson[19–23] based on Hopkins's[24] wave aberration theory and Buchroeder's[25] idea about aberration field decenter vector. It is a useful tool that contributes greatly to the study of the aberration field characteristics of optical systems involving misaligned, or intentionally decentered and tilted components. In recent years, NAT has been brought into applications in the field of optical design and alignment. Schmid et al.[26] studied the misalignment-induced nodal aberration fields for two-mirror astronomical telescopes using NAT. Thompson et al.[27] used NAT to describe the aberration field dependencies that arise in the presence of misalignments for TMA telescopes. Ju et al.[28] utilized NAT to study the misalignment-induced nodal aberration fields in off-axis TMA telescopes. Sebag et al.[29] made a Large Synoptic Survey Telescope (LSST) alignment plan based on NAT. Gu[30] aligned an on-axis TMA telescope using fifth-order NAT. Zhang[31] aligned an off-axis TMA telescope using fifth-order NAT.

Since off-axis TMA optical systems have many misalignment degrees of freedom, it is difficult to establish misalignment equations only using A222 and A131 in NAT. Therefore, the basic idea of the existing NAT-based CAA algorithm is to build a calculation model based on fifth-order NAT. To overcome the ill-conditioned characteristic of the fifth-order NAT solving equations, the tertiary mirror (TM) and image plane boresight errors [defined as the height of optical axis ray (OAR) on TM and image plane] were introduced.[30,31] The calculation procedure of this method is completely feasible in theory, and misalignments of each mirror could be accurately calculated. However, when considering practical engineering applications, the measurement noise of high-order Zernike coefficients is relatively large, and the actual measurement methods and measurement accuracy of boresight errors are subject to further investigation. These reasons lead to the poor robustness of the fifth-order NAT misalignment calculation model (FNCM),[30,31] and it is thus difficult for the model to meet the needs of practical engineering applications.

In this paper, we take an off-axis TMA optical system with designed tilts and decenters as the research object, a misalignment calculation model based on quadratic aberration field decenter vectors is constructed for verifying the alignment methods of CSST. Compared with the FNCM, the constructed third-order quadratic NAT calculation model (TNCM) tactically avoids the measurement of boresight errors. Moreover, TNCM is relatively simple, avoids the measurement of high-order Zernike coefficients, and shows higher robustness than FNCM. In Sec. 2, we describe the optical design parameters of the off-axis TMA optical system with designed tilts and decenters. In Sec. 3, for the off-axis TMA system with designed tilts and decenters, two concepts of inherent aberration field decenter vector and misalignment aberration field decenter vector are first introduced. The aberration field decenter vectors are then derived using the paraxial ray tracing method proposed by Buchroeder. In Sec. 4, for the off-axis TMA system with designed tilts and decenters, the relationship between the Fringe Zernike polynomial and third-order wave aberration expressions is derived, and TNCM is constructed using quadratic aberration field decenter vectors. In Sec. 5, the comparative experiments of simulation alignment with FNCM are carried out. In Sec. 6, the experimental results are discussed. We conclude in Sec. 7.

2 Design Parameters for the Pupil-Offset Off-Axis TMA Telescope with Designed Tilts and Decenters

To verify the key technologies such as optical design, optical index, alignment and test of CSST, a scaled-down verification system was developed, as shown in Fig. 2. The main design parameters are shown in Table 1.

The aperture stop is located on the primary mirror (PM) and is decentered relative to the PM. Both the secondary mirror (SM) and the third mirror (TM) contain decenters along the Y-direction and tilts around the X axis. The RMS WFE of the system's full FOV is basically below 0.0574 waves. Figure 3 shows the exit pupil aberrations and the corresponding Fringe Zernike coefficients (hereinafter referred to as Zernike coefficients) of nine typical FOVs when

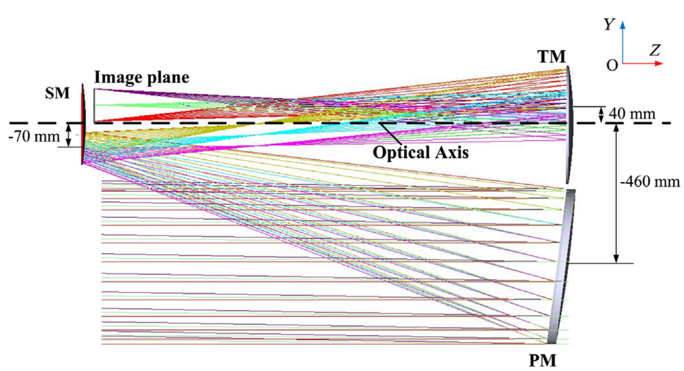

Fig. 2 The optical path of the off-axis TMA telescope with designed tilts and decenters.

Table 1 Specific optical parameters of the telescope.

Surface	Radius	Thickness	Conic Constant	Decenter *X* (mm)	Decenter *Y* (mm)	Tilt About *X* (deg)	Tilt About *Y* (deg)
Object	Infinity	Infinity	0	—	—	—	—
Stop	Infinity	0	0	—	−460	—	—
PM	−3600.410	−1551.770	−0.921	0	0	0	0
SM	−910.903	1558.700	−4.828	0	−1.401	0.175	0
TM	−1219.413	−1533.360	−0.292	0	−3.486	0.249	0
Image	Infinity	0	—	—	—	—	—
Effective focal length				6000 mm			
Entrance pupil				PM			
Entrance pupil diameter				500 mm			
Effective FOV				1 deg × 1 deg			
Central FOV				(0 deg,−0.5 deg)			

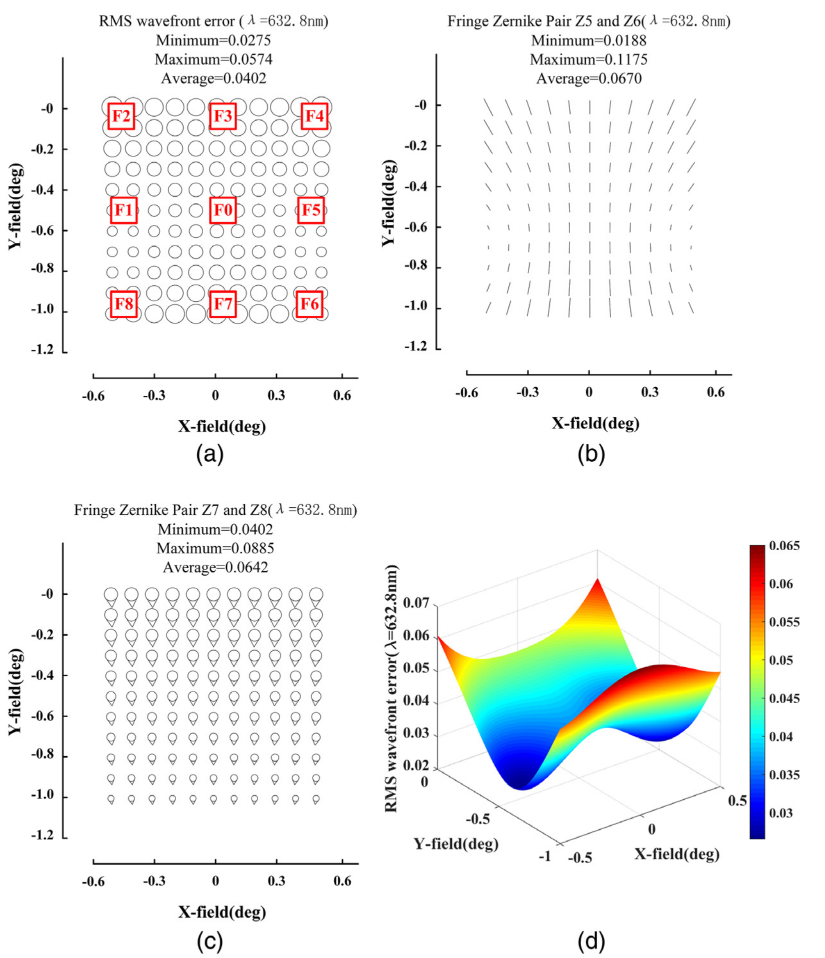

Fig. 3 Distribution of the aberrations of the wavefront, (a) two dimensional RMS WFE; (b) astigmatism; (c) coma; and (d) three dimensional RMS WFE in each FOV.

the optical system has no misalignment (Z5, Z6, Z7, and Z8 represent the Astig x, Astig y, Coma x, and Coma y, respectively).

3 Aberration Field Decenter Vectors for the Pupil-Offset Off-Axis TMA System with Designed Tilts and Decenters

3.1 *Effective Field Vector*

For the system in Sec. 2, when the designed decenters and tilts are zero, it can be regarded as an off-axis portion of a hypothetical axisymmetric coaxial system (hereinafter referred to as coaxial parent system). As shown in Figs. 4(a) and 4(c), the pupil of the off-axis TMA system is compressed and offset relative to the pupil of the coaxial parent system.

The following mathematical relationship can be established between the pupil of the off-axis TMA system and the pupil of the coaxial parent system.

$$\begin{cases} \vec{\rho}^{\#} = M \cdot \vec{\rho} + \vec{h} \\ M = \frac{r}{R} \end{cases} \tag{1}$$

In Eq. (1), M represents the scale factor of the aperture size of the off-axis portion relative to the coaxial parent pupil. r is the pupil radius of the off-axis TMA system, R stands for the pupil radius of the coaxial parent system. $\vec{h}$ denotes the normalized position change vector of the pupil center of the off-axis TMA system relative to its coaxial parent system. $\vec{\rho}^{\#}$ represents the normalized pupil vector of the coaxial parent system. $\vec{\rho}$ represents the normalized pupil vector of the off-axis TMA system.

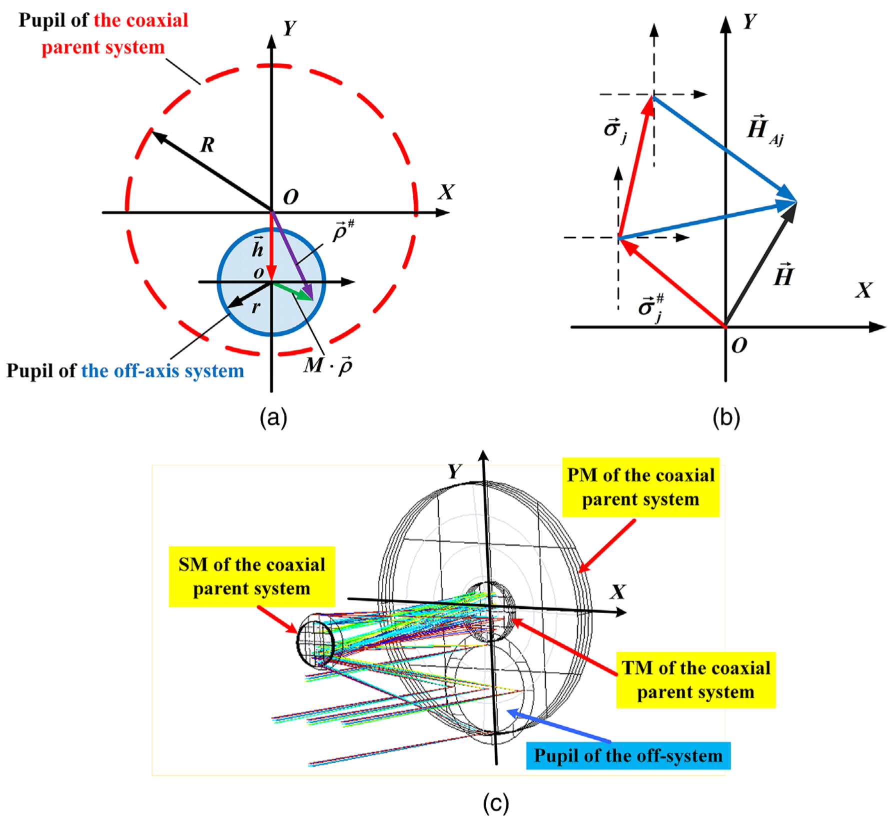

Fig. 4 (a) Coordinate transformation between the pupil of the off-axis TMA system and its coaxial parent system. (b) Field vector diagram of the misaligned off-axis TMA system. (c) The coaxial parent system.

For the off-axis TMA system, the symmetric center of the aberration field will shift due to the designed tilts and decenters of optical elements. The magnitude and direction of the decenter vector are denoted by $\vec{\sigma}_j^{\#}$, which refers to the inherent aberration field decenter vector of the system in this case. When the off-axis TMA optical system is misaligned, the symmetric center of the aberration field will be shifted again, and the magnitude and direction of the decenter vector are represented by $\vec{\sigma}_j$, which in this case refers to the misalignment aberration field decenter vector of the system. j represents different optical surfaces. As shown in Fig. 4(b), the normalized effective field vector of the system is

$$\vec{H}_{Aj} = \vec{H} - \vec{\sigma}_j^{\#} - \vec{\sigma}_j. \tag{2}$$

3.2 *Ray Tracing of Aberration Field Decenter Vectors*

The aberration field decenter vectors of each surface in the off-axis TMA system are determined using the paraxial ray tracing method of Buchroeder[25] under its corresponding coaxial parent system. The results can be obtained by tracing the chief ray of the marginal field and the OAR.[25] Some researchers have given the deduction conclusions,[29–31] but the specific ray tracing process and deduction ideas are mostly not discussed in detail. In this section, the coaxial parent system is taken as an example for a simple ray tracing (The ray tracing methods and derivation ideas are also applicable to other systems).

Buchroeder[25] traces the aberration field decenter vectors of a single misaligned surface according to Fig. 5 and the following equations:

$$\vec{\sigma}_j^{sph} = \begin{bmatrix} -\dfrac{(\vec{\bar{u}}_{OAR}^{\#})_{j,x} + (\vec{\bar{y}}_{OAR}^{\#})_{j,x} c_j - (\vec{\beta}^{\#})_{j,x} - c_j (\vec{\delta v}^{\#})_{j,x}}{\bar{u}_j + \bar{y}_j c_j} \\ -\dfrac{(\vec{\bar{u}}_{OAR}^{\#})_{j,y} + (\vec{\bar{y}}_{OAR}^{\#})_{j,y} c_j - (\vec{\beta}^{\#})_{j,y} - c_j (\vec{\delta v}^{\#})_{j,y}}{\bar{u}_j + \bar{y}_j c_j} \end{bmatrix}, \tag{3}$$

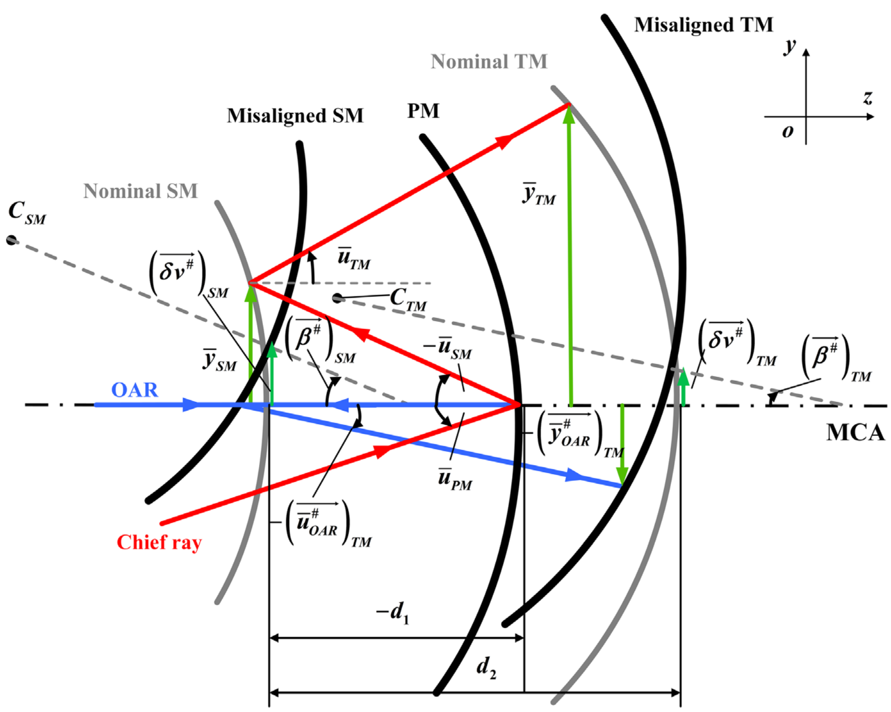

Fig. 5 The ray tracing process of OAR (blue) and the chief ray of the marginal field (red).

$$\vec{\sigma}_j^{asph} = \begin{bmatrix} \frac{(\delta\vec{v}^{\#})_{j,x}-(\vec{\overline{y}}^{\#}_{OAR})_{j,x}}{\overline{y}_j} \\ \frac{(\delta\vec{v}^{\#})_{j,y}-(\vec{\overline{y}}^{\#}_{OAR})_{j,y}}{\overline{y}_j} \end{bmatrix}. \tag{4}$$

In the above equations, $\vec{\sigma}^{sph}$ and $\vec{\sigma}^{asph}$ represent the aberration field decenter vectors of spherical and aspheric parts, respectively. c represents the curvature of the surfaces. $\vec{\overline{u}}^{\#}_{OAR}$ and $\vec{\overline{y}}^{\#}_{OAR}$ represent the incident angle and height of the OAR at each surface relative to the mechanical axis (MCA). The OAR is the ray that is emitted from the center of the FOV of the coaxial parent system and passes through the center of the entrance pupil before the pupil is decentered, but after the SM and the TM have been perturbed. $\overline{u}$ and $\overline{y}$ represent the incident angle and height of the chief ray of the marginal field at each surface relative to the MCA. The chief ray of the marginal field can also lies in the X-Z sagittal. $\delta\vec{v}^{\#}$ represents the decenters of the surfaces and defines the location of the vertices of the surfaces relative to the MCA. The vertices of the surfaces are the intersection of the surfaces and their axes of rotation. $\vec{\beta}^{\#}$ represents the tilts of the surfaces (measured from MCA). The subscripts x and y represent the sagittal and meridian vector components, respectively. It is worth noting that the ray tracing method holds for surfaces that are individually rotationally symmetric, though possibly decentered and/or tilted. However, for freeform surfaces that have no well-defined vertex location, the method is not applicable.

When misalignments are not introduced into the optical surfaces, the inherent aberration field decenter vectors, which is determined by the designed tilts and decenters, can be obtained by Eq. (3) and (4). When misalignments are introduced into the optical surfaces, the vector sum of inherent aberration field decenter vectors and misalignment aberration field decenter vectors can be obtained by Eqs. (3) and (4). The misalignment aberration field decenter vectors can thus be calculated according to Eq. (5).

$$\vec{\sigma}_j^{sum} = \vec{\sigma}_j^{\#} + \vec{\sigma}_j. \tag{5}$$

For the system in Sec. 2, all tilts and decenters of the SM and TM are referred to the PM optical axis, which refers to the optical axis of the coaxial parent system before the pupil is decentered and the SM and TM are perturbed. So in this paper, we use the PM as a datum for ray tracing, and assume it is fixed. On this basis, the aberration field decenter vectors of the off-axis TMA system can be derived by tracing three surfaces. Using above paraxial ray tracing method, its OAR and edge field chief ray can be traced, and the system's primary, secondary and third mirror aberration field decenter vector expressions can thus be obtained by Eqs. (3) and (4). As shown by the red line in Fig. 5, the chief ray of the marginal field is traced.

$$\overline{u}_{SM} = -\overline{u}_{PM}, \quad \overline{y}_{SM} = -d_1\overline{u}_{PM}, \tag{6}$$

$$\overline{u}_{TM} = (1 + 2d_1c_{SM})\overline{u}_{PM}, \quad \overline{y}_{TM} = [d_1(2c_{SM}d_2 - 1) + d_2]\overline{u}_{PM}, \tag{7}$$

where the subscripts PM, SM, and TM of each item represent the primary mirror, the secondary mirror, and the third mirror, respectively. d_1 represents the axial distance between the SM and the PM. d_2 represents the axial distance between the SM and the TM.

Then the OAR is traced, as shown by the blue line in Fig. 5.

$$(\vec{\overline{u}}^{\#}_{OAR})_{SM} = \begin{bmatrix} 0 \\ 0 \end{bmatrix}, \quad (\vec{\overline{y}}^{\#}_{OAR})_{SM} = \begin{bmatrix} 0 \\ 0 \end{bmatrix}, \tag{8}$$

$$(\vec{\overline{u}}^{\#}_{OAR})_{TM} = -2\begin{bmatrix} (\vec{\overline{u}}^{\#}_{OAR})_{SM,x} + c_{SM}(\vec{\overline{y}}^{\#}_{OAR})_{SM,x} - (\vec{\beta}^{\#})_{SM,x} - c_{SM}(\delta\vec{v}^{\#})_{SM,x} \\ (\vec{\overline{u}}^{\#}_{OAR})_{SM,y} + c_{SM}(\vec{\overline{y}}^{\#}_{OAR})_{SM,y} - (\vec{\beta}^{\#})_{SM,y} - c_{SM}(\delta\vec{v}^{\#})_{SM,y} \end{bmatrix}, \tag{9}$$

$$(\vec{\bar{y}}^{\#}_{OAR})_{TM} = d_2 \begin{bmatrix} (\vec{\bar{u}}^{\#}_{OAR})_{TM,x} \\ (\vec{\bar{u}}^{\#}_{OAR})_{TM,y} \end{bmatrix}. \tag{10}$$

By substituting Eqs. (6), (7), (8), (9), and (10) into Eqs. (3) and (4), the below expressions are derived.

$$\begin{cases} \vec{\sigma}^{sph}_{PM} = \begin{bmatrix} 0 \\ 0 \end{bmatrix} \\ \vec{\sigma}^{asph}_{PM} = \begin{bmatrix} 0 \\ 0 \end{bmatrix} \\ \vec{\sigma}^{sph}_{SM} = \begin{bmatrix} -\dfrac{(\vec{\bar{u}}^{\#}_{OAR})_{SM,x} + c_{SM}(\vec{\bar{y}}^{\#}_{OAR})_{SM,x} - (\vec{\beta}^{\#})_{SM,x} - c_{SM}(\delta\vec{v}^{\#})_{SM,x}}{\bar{u}_{SM} + \bar{y}_{SM} c_{SM}} \\ -\dfrac{(\vec{\bar{u}}^{\#}_{OAR})_{SM,y} + c_{SM}(\vec{\bar{y}}^{\#}_{OAR})_{SM,y} c_{SM} - -(\vec{\beta}^{\#})_{SM,y} - c_{SM}(\delta\vec{v}^{\#})_{SM,y}}{\bar{u}_{SM} + \bar{y}_{SM} c_{SM}} \end{bmatrix} = \begin{bmatrix} \dfrac{-c_{SM} XDE_{SM} + BDE_{SM}}{(1 + c_{SM} d_1)\bar{u}_{PM}} \\ \dfrac{-c_{SM} YDE_{SM} - ADE_{SM}}{(1 + c_{SM} d_1)\bar{u}_{PM}} \end{bmatrix} \\ \vec{\sigma}^{asph}_{SM} = \begin{bmatrix} \dfrac{(\delta\vec{v}^{\#})_{SM,x} - (\vec{\bar{y}}^{\#}_{OAR})_{SM,x}}{\bar{y}_{SM}} \\ \dfrac{(\delta\vec{v}^{\#})_{SM,y} - (\vec{\bar{y}}^{\#}_{OAR})_{SM,y}}{\bar{y}_{SM}} \end{bmatrix} = \begin{bmatrix} \dfrac{-XDE_{SM}}{d_1 \bar{u}_{PM}} \\ \dfrac{-YDE_{SM}}{d_1 \bar{u}_{PM}} \end{bmatrix} \\ \vec{\sigma}^{sph}_{TM} = \begin{bmatrix} -\dfrac{(\vec{\bar{u}}^{\#}_{OAR})_{TM,x} + c_{TM}(\vec{\bar{y}}^{\#}_{OAR})_{TM,x} - (\vec{\beta}^{\#})_{TM,x} - c_{TM}(\delta\vec{v}^{\#})_{TM,x}}{\bar{u}_{TM} + \bar{y}_{TM} c_{TM}} \\ -\dfrac{(\vec{\bar{u}}^{\#}_{OAR})_{TM,y} + c_{TM}(\vec{\bar{y}}^{\#}_{OAR})_{TM,y} - (\vec{\beta}^{\#})_{TM,y} - c_{TM}(\delta\vec{v}^{\#})_{TM,y}}{\bar{u}_{TM} + \bar{y}_{TM} c_{TM}} \end{bmatrix} \\ \quad = \begin{bmatrix} \dfrac{-2(1 + c_{TM} d_2)(c_{SM} XDE_{SM} - BDE_{SM}) + c_{TM} XDE_{TM} - BDE_{TM}}{[1 + 2c_{SM}(c_{TM} d_1 d_2 + d_1) + c_{TM}(d_2 - d_1)]\bar{u}_{PM}} \\ \dfrac{-2(1 + c_{TM} d_2)(c_{SM} YDE_{SM} + ADE_{SM}) + c_{TM} YDE_{TM} + ADE_{TM}}{[1 + 2c_{SM}(c_{TM} d_1 d_2 + d_1) + c_{TM}(d_2 - d_1)]\bar{u}_{PM}} \end{bmatrix} \\ \vec{\sigma}^{asph}_{TM} = \begin{bmatrix} \dfrac{(\delta\vec{v}^{\#})_{TM,x} - (\vec{\bar{y}}^{\#}_{OAR})_{TM,x}}{\bar{y}_{TM}} \\ \dfrac{(\delta\vec{v}^{\#})_{TM,y} - (\vec{\bar{y}}^{\#}_{OAR})_{TM,y}}{\bar{y}_{TM}} \end{bmatrix} = \begin{bmatrix} \dfrac{-2d_2(c_{SM} XDE_{SM} - BDE_{SM}) + XDE_{TM}}{[d_1(2c_{SM} d_2 - 1) + d_2]\bar{u}_{PM}} \\ \dfrac{-2d_2(c_{SM} YDE_{SM} + ADE_{SM}) + YDE_{TM}}{[d_1(2c_{SM} d_2 - 1) + d_2]\bar{u}_{PM}} \end{bmatrix} \end{cases}, \tag{11}$$

where ADE and BDE represent the amount of tilt of each optical surface around x axis and y axis, respectively. XDE and YDE represent the amount of decenter of each optical surface in x direction and y direction, respectively. ADE and BDE are related to $\vec{\beta}^{\#}$. XDE and YDE are related to $\delta\vec{v}^{\#}$ (their specific meanings can be referred to in Refs. 25 and 32).

4 Calculation Algorithm of Misalignment

In the actual alignment process, the exit pupil WFE of an optical system is usually fitted into a Zernike polynomial.[33] Therefore, this paper derives the relationship between the Fringe Zernike polynomial and third-order wave aberration expressions of the misaligned off-axis system to solve the system's misalignments. By expanding the first nine terms of the Fringe Zernike polynomial[34] in sequence, we get

$$\begin{aligned} W(H_x, H_y, |\rho|, \phi) &= C_1(H_x, H_y) + C_2(H_x, H_y)|\rho| \cos\phi \\ &+ C_3(H_x, H_y)|\rho| \sin\phi + C_4(H_x, H_y)(2|\rho|^2 - 1) \\ &+ C_5(H_x, H_y)|\rho|^2 \cos 2\phi + C_6(H_x, H_y)|\rho|^2 \sin 2\phi \\ &+ C_7(H_x, H_y)(3|\rho|^3 - 2|\rho|)\cos\phi + C_8(H_x, H_y)(3|\rho|^3 - 2|\rho|)\sin\phi \\ &+ C_9(H_x, H_y)(6|\rho|^4 - 6|\rho|^2 + 1), \end{aligned} \tag{12}$$

where terms 5 to 9 correspond to third-order wave aberrations.

For the misaligned off-axis TMA system, the existing fifth-order NAT algorithm are mostly based on high-order Zernike coefficients and boresight errors.[30,31] Due to the introduction of high-order Zernike coefficients, the mathematical and physical model between misalignments and high-order aberrations of the system is extremely complicated. The resulting equations for solving misalignments are often ill-conditioned. When measurement noise is taken into account, the calculated results of misalignments will often not converge due to the influence of the ill-conditioned equations and may even differ greatly from the actual results. In addition, it is difficult to measure the boresight errors introduced by the fifth-order NAT algorithm in practical engineering application. To solve the above problems, third-order astigmatism and third-order coma are used to establish a misalignment calculation model based on quadratic aberration field decenter vectors. The process is as follows:

Thompson[20] derived third-order wave aberration expressions of misaligned axisymmetric coaxial optical systems (on-axis systems), where third-order astigmatism, third-order coma, and third-order spherical expressions are given as

$$\begin{cases} W_{on-axis}^{Astig} = \frac{1}{2}\left[\sum_j W_{222j}\vec{H}_n^2 - 2\vec{H}_n\left(\sum_j W_{222j}\vec{\sigma}_j\right) + \sum_j W_{222j}\vec{\sigma}_j^2\right]\cdot\vec{\rho}^2 \\ W_{on-axis}^{Coma} = \left\{\left[\left(\sum_j W_{131j}\vec{H}_n\right) - \sum_j W_{131j}\vec{\sigma}_j\right]\cdot\vec{\rho}\right\}(\vec{\rho}\cdot\vec{\rho}) \\ W_{on-axis}^{Sph} = \sum_j W_{040j}(\vec{\rho}\cdot\vec{\rho})^2 \end{cases}, \tag{13}$$

where n represents different FOVs, j represents different optical surfaces. For the off-axis system in Sec. 2, its hypothetical coaxial parent system is what Thompson discussed. On this basis, substitute $\vec{\sigma}_j$, $\vec{\rho}$ for $\vec{\sigma}_j^{\#} + \vec{\sigma}_j$, $M\cdot\vec{\rho} + \vec{h}$, respectively, and the third-order astigmatism expression of the misaligned off-axis system is expressed as

$$\begin{aligned} W_{off-axis}^{Astig} &= \frac{1}{2}\left\{\sum_j W_{222j}\vec{H}_n^2 - 2\vec{H}_n\left[\sum_j W_{222j}(\vec{\sigma}_j^{\#} + \vec{\sigma}_j)\right] + \sum_j W_{222j}(\vec{\sigma}_j^{\#} + \vec{\sigma}_j)^2\right\}\cdot(M\cdot\vec{\rho} + \vec{h})^2, \\ &= \frac{1}{2}\left\{\sum_j W_{222j}\vec{H}_n^2 - 2\vec{H}_n\left[\sum_j W_{222j}(\vec{\sigma}_j^{\#} + \vec{\sigma}_j)\right] + \sum_j W_{222j}[(\vec{\sigma}_j^{\#})^2 + (\vec{\sigma}_j)^2] \right. \\ &\quad \left. + 2\sum_j W_{222j}\vec{\sigma}_j^{\#}\vec{\sigma}_j\right\}\cdot(M\cdot\vec{\rho} + \vec{h})^2. \end{aligned} \tag{14}$$

Let

$$\begin{cases} \vec{A}_{222,n} = \vec{H}_n\sum_j W_{222j}(\vec{\sigma}_j^{\#} + \vec{\sigma}_j) \\ \vec{B}_{222}^2 = \sum_j W_{222j}[(\vec{\sigma}_j^{\#})^2 + (\vec{\sigma}_j)^2](\vec{\rho}\cdot\vec{\rho}) \\ \vec{C}_{222} = \sum_j W_{222j}\vec{\sigma}_j^{\#}\vec{\sigma}_j \\ \vec{W}_{222,n} = \vec{H}_n^2\sum_j W_{222j} \end{cases},$$

then Eq. (14) can be simplified as

$$W_{off-axis}^{Astig} == \frac{1}{2}(\vec{W}_{222,n} - 2\vec{A}_{222,n} + \vec{B}_{222}^2 + 2\vec{C}_{222})\cdot(M\cdot\vec{\rho} + \vec{h})^2. \tag{15}$$

Since piston, tilt and defocus have no practical contribution to solving misalignments in NAT, they can be ignored. According to the vector multiplication of NAT, we can expand Eq. (15), and get

$$W_{off-axis}^{Astig} = M^2 \begin{bmatrix} -\vec{A}_{222,xn} + \frac{\vec{B}^2_{222,x}}{2} + \vec{C}_{222x} + \frac{\vec{W}_{222,xn}}{2} \\ -\vec{A}_{222,yn} + \frac{\vec{B}^2_{222,y}}{2} + \vec{C}_{222y} + \frac{\vec{W}_{222,yn}}{2} \end{bmatrix} \cdot \begin{bmatrix} |\vec{\rho}|^2 \cos(2\phi) \\ |\vec{\rho}|^2 \sin(2\phi) \end{bmatrix}. \tag{16}$$

At this point, it can be found that after expanding the third-order astigmatism expression, we could compare Eqs. (16) and (12), and get

$$W_{off-axis}^{Astig} = C_5(H_{xn}, H_{yn})|\rho|^2 \cos 2\phi + C_6(H_{xn}, H_{yn})|\rho|^2 \sin 2\phi. \tag{17}$$

It can be seen from Eqs. (16) and (17) that the third-order astigmatism expression of the misaligned off-axis system derives the same type of aberration terms as the hypothetical coaxial parent system.

The third-order coma expression of the misaligned off-axis system is expressed as

$$W_{off-axis}^{Coma} = \left\{ \left[\left(\sum_j W_{131j} \vec{H}_n \right) - \sum_j W_{131j} (\vec{\sigma}_j^{\#} + \vec{\sigma}_j) \right] \cdot (M \cdot \vec{\rho} + \vec{h}) \right\} (M \cdot \vec{\rho} + \vec{h}) \cdot (M \cdot \vec{\rho} + \vec{h}). \tag{18}$$

Let

$$\begin{cases} \vec{A}_{131} = \sum_j W_{131j} (\vec{\sigma}_j^{\#} + \vec{\sigma}_j) \\ \vec{W}_{131,n} = \sum_j W_{131j} \vec{H}_n \end{cases}.$$

Then according to the vector multiplication of NAT, we can expand Eq. (18), and get

$$W_{off-axis}^{Coma} = \begin{bmatrix} M^2 h_y (-\vec{W}_{131,yn} + \vec{A}_{131,y}) \\ M^2 h_y (\vec{W}_{131,xn} - \vec{A}_{131,x}) \end{bmatrix} \cdot \begin{bmatrix} |\rho|^2 \cos 2\phi \\ |\rho|^2 \sin 2\phi \end{bmatrix} + \begin{bmatrix} \frac{M^3}{3} (\vec{W}_{131,xn} - \vec{A}_{131,x}) \\ \frac{M^3}{3} (\vec{W}_{131,yn} - \vec{A}_{131,y}) \end{bmatrix} \cdot \begin{bmatrix} (3|\rho|^3 - 2|\rho|) \cos \phi \\ (3|\rho|^3 - 2|\rho|) \sin \phi \end{bmatrix}. \tag{19}$$

For the off-axis system in Fig. 2, the physical meaning of the meridian direction and sagittal direction of the pupil center position change vector is the same, so let $h_x = 0$ in Eq. (19). At this point, after expanding the third-order coma expression and by comparing Eqs. (19) and (12), it can be obtained that

$$W_{off-axis}^{Coma} = C_5(H_x, H_y)|\rho|^2 \cos 2\phi + C_6(H_x, H_y)|\rho|^2 \sin 2\phi + C_7(H_x, H_y)(3|\rho|^3 - 2|\rho|) \cos \phi + C_8(H_x, H_y)(3|\rho|^3 - 2|\rho|) \sin \phi. \tag{20}$$

It can be seen from Eqs. (19) and (20) that the third-order coma expression of the misaligned off-axis system not only derives the same type of third-order coma terms as the hypothetical coaxial parent system but also derives the same type of third-order astigmatism terms.

The third-order spherical aberration expression of the misaligned off-axis system is expressed as

$$W_{off-axis}^{Sph} = \sum_j W_{040j} [(M\vec{\rho} + \vec{h}) \cdot (M\vec{\rho} + \vec{h})]^2. \tag{21}$$

In the same way, according to the vector multiplication of NAT, Eq. (21) can finally be expanded as

$$W_{off-axis}^{Sph} = \frac{M^4}{6}\sum_j W_{040j}(6|\rho|^4 - 6|\rho|^2 + 1) + \frac{4M^3 h_y}{3}\sum_j W_{040j}[(3|\rho|^3 - 2|\rho|)\sin\phi] \\ -2M^2 h_y^2 \sum_j W_{040j}|\rho|^2 \cos 2\phi. \tag{22}$$

By comparing Eqs. (12) and (22), it can be obtained that

$$W_{off-axis}^{Sph} = C_9(H_x, H_y)(6|\rho|^4 - 6|\rho|^2 + 1) \\ + C_8(H_x, H_y)(3|\rho|^3 - 2|\rho|)\sin\phi C_5(H_x, H_y)|\rho|^2 \cos 2\phi. \tag{23}$$

It can be seen from Eqs. (22) and (23) that the third-order spherical aberration expression of the misaligned off-axis system not only derives the same type of third-order spherical aberration term as the hypothetical coaxial parent system but also derives the same type of third-order coma and third-order astigmatism terms.

Equations (17), (20), and (23) are the final derivation results, for which the following conclusions can be drawn.

For the misaligned off-axis system, the third-order wave aberrations that contribute to the fifth and sixth terms of the Fringe Zernike polynomial include third-order astigmatism, third-order coma, and third-order spherical aberration. The third-order wave aberrations that contribute to the seventh and eighth terms of the Fringe Zernike polynomial include third-order coma and third-order spherical aberration. By sorting out Eqs. (16), (17), (19), (20), (22), and (23), the misalignment calculation model of the misaligned off-axis TMA system based on NAT can be obtained.

$$\begin{bmatrix} -M^2 & 0 & \frac{M^2}{2} & 0 & M^2 & 0 & 0 & 0 \\ 0 & -M^2 & 0 & \frac{M^2}{2} & 0 & M^2 & 0 & 0 \\ 0 & 0 & 0 & 0 & 0 & 0 & -\frac{M^3}{3} & 0 \\ 0 & 0 & 0 & 0 & 0 & 0 & 0 & -\frac{M^3}{3} \end{bmatrix} \begin{bmatrix} \vec{A}_{222,xn} \\ \vec{A}_{222,yn} \\ \vec{B}^2_{222,x} \\ \vec{B}^2_{222,y} \\ \vec{C}_{222,x} \\ \vec{C}_{222,y} \\ \vec{A}_{131,x} \\ \vec{A}_{131,y} \end{bmatrix} = K \begin{bmatrix} C_5(H_{xn}, H_{yn}) - \frac{M^2 \vec{W}_{222,xn}}{2} \\ C_6(H_{xn}, H_{yn}) - \frac{M^2 \vec{W}_{222,yn}}{2} \\ C_7(H_{xn}, H_{yn}) - \frac{M^3 \vec{W}_{131,xn}}{3} \\ C_8(H_{xn}, H_{yn}) - \frac{M^3 \vec{W}_{131,yn}}{3} \\ C_9(H_{xn}, H_{yn}) \end{bmatrix}, \tag{24}$$

$$K = \begin{bmatrix} 1 & 0 & 0 & 3\frac{h_y}{M} & \left(12 - 24\frac{h_y}{M}\right)\frac{h_y}{M} \\ 0 & 1 & -3\frac{h_y}{M} & 0 & 0 \\ 0 & 0 & 1 & 0 & 0 \\ 0 & 0 & 0 & 1 & -8\frac{h_y}{M} \end{bmatrix}. \tag{25}$$

In the Eq. (24), expand $\vec{A}_{222,xn}$, $\vec{A}_{222,yn}$, $\vec{B}^2_{222,x}$, $\vec{B}^2_{222,y}$, $\vec{C}_{222,x}$ $\vec{C}_{222,y}$, $\vec{A}_{131,x}$, $\vec{A}_{131,y}$, $\vec{W}_{222,xn}$, $\vec{W}_{222,yn}$, $\vec{W}_{131,xn}$, $\vec{W}_{131,yn}$, and we get

$$\begin{cases} \vec{A}_{222,xn} = H_{xn}\left[\begin{array}{l} W_{222,SM}^{sph}(\vec{\sigma}_{SM,x}^{\#,sph} + \vec{\sigma}_{SM,x}^{sph}) + W_{222,SM}^{asph}(\vec{\sigma}_{SM,x}^{\#,asph} + \vec{\sigma}_{SM,x}^{asph}) \\ +W_{222,TM}^{sph}(\vec{\sigma}_{TM,x}^{\#,sph} + \sigma_{TM,x}^{sph}) + W_{222,TM}^{asph}(\vec{\sigma}_{TM,x}^{\#,asph} + \vec{\sigma}_{TM,x}^{asph}) \end{array}\right] \\ -H_{yn}\left[\begin{array}{l} W_{222,SM}^{sph}(\vec{\sigma}_{SM,y}^{\#,sph} + \sigma_{SM,y}^{sph}) + W_{222,SM}^{asph}(\vec{\sigma}_{SM,y}^{\#,asph} + \vec{\sigma}_{SM,y}^{asph}) \\ +W_{222,TM}^{sph}(\vec{\sigma}_{TM,y}^{\#,sph} + \sigma_{TM,y}^{sph}) + W_{222,TM}^{asph}(\vec{\sigma}_{TM,y}^{\#,asph} + \vec{\sigma}_{TM,y}^{asph}) \end{array}\right] \\ \vec{A}_{222,yn} = H_{yn}\left[\begin{array}{l} W_{222,SM}^{sph}(\vec{\sigma}_{SM,x}^{\#,sph} + \vec{\sigma}_{SM,x}^{sph}) + W_{222,SM}^{asph}(\vec{\sigma}_{SM,x}^{\#,asph} + \vec{\sigma}_{SM,x}^{asph}) \\ +W_{222,TM}^{sph}(\vec{\sigma}_{TM,x}^{\#,sph} + \vec{\sigma}_{TM,x}^{sph}) + W_{222,TM}^{asph}(\vec{\sigma}_{TM,x}^{\#,asph} + \vec{\sigma}_{TM,x}^{asph}) \end{array}\right] \\ +H_{xn}\left[\begin{array}{l} W_{222,SM}^{sph}(\vec{\sigma}_{SM,y}^{\#,sph} + \vec{\sigma}_{SM,y}^{sph}) + W_{222,SM}^{asph}(\vec{\sigma}_{SM,y}^{\#,asph} + \vec{\sigma}_{SM,y}^{asph}) \\ +W_{222,TM}^{sph}(\vec{\sigma}_{TM,y}^{\#,sph} + \vec{\sigma}_{TM,y}^{sph}) + W_{222,TM}^{asph}(\vec{\sigma}_{TM,y}^{\#,asph} + \vec{\sigma}_{TM,y}^{asph}) \end{array}\right] \end{cases}, \tag{26}$$

$$\begin{cases} \vec{B}_{222,x} = W_{222,SM}^{sph}[(\vec{\sigma}_{SM,x}^{\#,sph})^2 - (\vec{\sigma}_{SM,y}^{\#,sph})^2 + (\vec{\sigma}_{SM,x}^{sph})^2 - (\vec{\sigma}_{SM,y}^{sph})^2] \\ +W_{222,SM}^{asph}[(\vec{\sigma}_{SM,x}^{\#,asph})^2 - (\vec{\sigma}_{SM,y}^{\#,asph})^2 + (\vec{\sigma}_{SM,x}^{asph})^2 - (\vec{\sigma}_{SM,y}^{asph})^2] \\ +W_{222,TM}^{sph}[(\vec{\sigma}_{TM,x}^{\#,sph})^2 - (\vec{\sigma}_{TM,y}^{\#,sph})^2 + (\vec{\sigma}_{TM,x}^{sph})^2 - (\vec{\sigma}_{TM,y}^{sph})^2] \\ +W_{222,TM}^{asph}[(\vec{\sigma}_{TM,x}^{\#,asph})^2 - (\vec{\sigma}_{TM,y}^{\#,asph})^2 + (\vec{\sigma}_{TM,x}^{asph})^2 - (\vec{\sigma}_{TM,y}^{asph})^2] \\ \vec{B}_{222,y} = 2W_{222,SM}^{sph}[(\vec{\sigma}_{SM,x}^{\#,sph})(\vec{\sigma}_{SM,y}^{\#,sph}) + (\vec{\sigma}_{SM,x}^{sph})(\vec{\sigma}_{SM,y}^{sph})] \\ +2W_{222,SM}^{asph}[(\vec{\sigma}_{SM,x}^{\#,asph})(\vec{\sigma}_{SM,y}^{\#,asph}) + (\vec{\sigma}_{SM,x}^{asph})(\vec{\sigma}_{SM,y}^{asph})] \\ +2W_{222,TM}^{sph}[(\vec{\sigma}_{TM,x}^{\#,sph})(\vec{\sigma}_{TM,y}^{\#,sph}) + (\vec{\sigma}_{TM,x}^{sph})(\vec{\sigma}_{TM,y}^{sph})] \\ +2W_{222,TM}^{asph}[(\vec{\sigma}_{TM,x}^{\#,asph})(\vec{\sigma}_{TM,y}^{\#,asph}) + (\vec{\sigma}_{TM,x}^{asph})(\vec{\sigma}_{TM,y}^{asph})] \end{cases}, \tag{27}$$

$$\begin{cases} \vec{C}_{222,x} = W_{222,SM}^{sph}[(\vec{\sigma}_{SM,x}^{\#,sph})(\vec{\sigma}_{SM,x}^{sph}) - (\vec{\sigma}_{SM,y}^{\#,sph})(\vec{\sigma}_{SM,y}^{sph})] \\ +W_{222,SM}^{asph}[(\vec{\sigma}_{SM,x}^{\#,asph})(\vec{\sigma}_{SM,x}^{asph}) - (\vec{\sigma}_{SM,y}^{\#,asph})(\vec{\sigma}_{SM,y}^{asph})] \\ +W_{222,TM}^{sph}[(\vec{\sigma}_{TM,x}^{\#,sph})(\vec{\sigma}_{TM,x}^{sph}) - (\vec{\sigma}_{TM,y}^{\#,sph})(\vec{\sigma}_{TM,y}^{sph})] \\ +W_{222,TM}^{asph}[(\vec{\sigma}_{TM,x}^{\#,asph})(\vec{\sigma}_{TM,x}^{asph}) - (\vec{\sigma}_{TM,y}^{\#,asph})(\vec{\sigma}_{TM,y}^{asph})] \\ \vec{C}_{222,y} = W_{222,SM}^{sph}[(\vec{\sigma}_{SM,y}^{\#,sph})(\vec{\sigma}_{SM,x}^{sph}) + (\vec{\sigma}_{SM,x}^{\#,sph})(\vec{\sigma}_{SM,y}^{sph})] \\ +W_{222,SM}^{asph}[(\vec{\sigma}_{SM,y}^{\#,asph})(\vec{\sigma}_{SM,x}^{asph}) + (\vec{\sigma}_{SM,x}^{\#,asph})(\vec{\sigma}_{SM,y}^{asph})] \\ +W_{222,TM}^{sph}[(\vec{\sigma}_{TM,y}^{\#,sph})(\vec{\sigma}_{TM,x}^{sph}) + (\vec{\sigma}_{TM,x}^{\#,sph})(\vec{\sigma}_{TM,y}^{sph})] \\ +W_{222,TM}^{asph}[(\vec{\sigma}_{TM,y}^{\#,asph})(\vec{\sigma}_{TM,x}^{asph}) + (\vec{\sigma}_{TM,x}^{\#,asph})(\vec{\sigma}_{TM,y}^{asph})] \end{cases}, \tag{28}$$

$$\begin{cases} \vec{A}_{131,x} = W_{131,SM}^{sph}(\vec{\sigma}_{SM,x}^{\#,sph} + \vec{\sigma}_{SM,x}^{sph}) + W_{131,SM}^{asph}(\vec{\sigma}_{SM,x}^{\#,asph} + \vec{\sigma}_{SM,x}^{asph}) \\ +W_{131,TM}^{sph}(\vec{\sigma}_{TM,x}^{\#,sph} + \sigma_{TM,x}^{sph}) + W_{131,TM}^{asph}(\vec{\sigma}_{TM,x}^{\#,asph} + \vec{\sigma}_{TM,x}^{asph}) \\ \vec{A}_{131,y} = W_{131,SM}^{sph}(\vec{\sigma}_{SM,y}^{\#,sph} + \vec{\sigma}_{SM,y}^{sph}) + W_{131,SM}^{asph}(\vec{\sigma}_{SM,y}^{\#,asph} + \vec{\sigma}_{SM,y}^{asph}) \\ +W_{131,TM}^{sph}(\vec{\sigma}_{TM,y}^{\#,sph} + \vec{\sigma}_{TM,y}^{sph}) + W_{131,TM}^{asph}(\vec{\sigma}_{TM,y}^{\#,asph} + \vec{\sigma}_{TM,y}^{asph}) \end{cases}, \tag{29}$$

$$\begin{cases} \vec{W}_{222,xn} = (W_{222,SM}^{sph} + W_{222,SM}^{asph} + W_{222,TM}^{sph} + W_{222,TM}^{asph})(H_{xn}^2 - H_{yn}^2) \\ \vec{W}_{222,yn} = 2(W_{222,SM}^{sph} + W_{222,SM}^{asph} + W_{222,TM}^{sph} + W_{222,TM}^{asph})H_{yn}H_{xn} \end{cases}. \tag{30}$$

In the above equations, $W_{222,SM}^{sph}$, $W_{222,SM}^{asph}$, $W_{222,TM}^{sph}$, $W_{222,TM}^{asph}$, $W_{131,SM}^{sph}$, $W_{131,SM}^{asph}$, $W_{131,TM}^{sph}$, and $W_{131,TM}^{asph}$ are the third-order aberration coefficients of the secondary and third mirrors in the coaxial parent system, which can be derived and calculated according to the Gauss parameters of the optical design. $\sigma_{SM,x}^{sph\#}$, $\sigma_{SM,x}^{asph\#}$, $\sigma_{TM,x}^{sph\#}$, $\sigma_{TM,x}^{asph\#}$, $\sigma_{SM,y}^{sph\#}$, $\sigma_{SM,y}^{asph\#}$, $\sigma_{TM,y}^{sph\#}$, and $\sigma_{TM,y}^{asph\#}$ are the inherent aberration field decenter vectors of the misaligned off-axis TMA optical system, which can be calculated according to Eq. (11). According to the overdetermined system of 8-element quadratic equations formed by Eqs. (24)–(30), using least squares algorithm, the misalignment aberration field decenter vectors can be solved. Finally, the solution to misalignments could be reached by combining Eq. (11). In actual alignment, only low-order Zernike coefficients corresponding to different FOVs need to be measured to apply the algorithm.

Compared with the misalignment calculation algorithm based on fifth-order NAT, this new algorithm effectively avoids the measurement of high-order Zernike coefficients and boresight errors and greatly reduces the complexity of the calculation process.

5 Computer-Aided Alignment Comparison Experiments

To verify the correctness of TNCM, Monte-Carlo comparison experiments are carried out with the existing FNCM for the off-axis TMA space telescope in Sec. 2, using the dynamic data linking function of MATLAB and ZEMAX software. FNCM is based on high-order Zernike coefficients and boresight errors. The third-order aberration coefficients of the secondary and third mirrors in the coaxial parent system can be calculated, as shown in Table 2.

5.1 *Simulation Alignment Without Measurement Noise*

In experiments, as shown in Fig. 3(a), five FOVS: F0 (0,−0.5), F2(−0.5,0), F4(0.5, 0), F6(0.5, −1), and F8 $(-0.5, -1)$ are selected at first. Their normalized radius is 1.12. Then, according to Eqs. (23)–(29) and Eq. (10), the simulation alignment experiments of the system can be conducted. In experiments, three types of misalignment error ranges are introduced into the SM and TM of the optical system, as shown in Table 3. In each misalignment error range, 500 sets of misalignments are randomly generated according to a standard uniform distribution, and these misalignments are introduced into the optical system, respectively. The misalignments are then calculated using the constructed TNCM and the existing FNCM. The correctness of the models is verified by comparing the introduced misalignments with the calculated misalignments. The comparison verification experiments process is shown in Fig. 6.

When there is no Zernike coefficients and boresight errors measurement noise, the calculation results are shown in Figs. 7, 8, and 9. The abscissa of the coordinate system in figures represents the simulated values of the misalignments, and the ordinate represents the calculated values of the misalignments.

The simulation results in Figs. 7, 8, and 9 show that the calculation results of TNCM and FNCM are not greatly affected by the range of misalignment error. However, with the significant increase of the misalignment error ranges, the calculation accuracy of FNCM is slightly higher than that of TNCM.

To further evaluate the calculation accuracy of TNCM and FNCM, the following formula is used to define the root-mean-square deviation (RMSD) of each misalignment degree of freedom.

Table 2 The third-order wave aberration coefficients of the SM and TM in the coaxial parent system.

$W_{131,SM}^{sph}$	$W_{131,SM}^{asph}$	$W_{131,TM}^{sph}$	$W_{131,TM}^{asph}$	$W_{222,SM}^{sph}$	$W_{222,SM}^{asph}$	$W_{222,TM}^{sph}$	$W_{222,TM}^{asph}$
400.96	457.43	188.86	397.48	−89.36	171.32	195.59	−436.21

Table 3 Three types of misalignment error ranges.

	XDE/YDE (SM,TM)	ADE/BDE (SM,TM)
Range 1	[−0.1,0.1]	[−0.01,0.01]
Range 2	[−0.2,0.2]	[−0.02,0.02]
Range 3	[−0.3,0.3]	[−0.03,0.03]

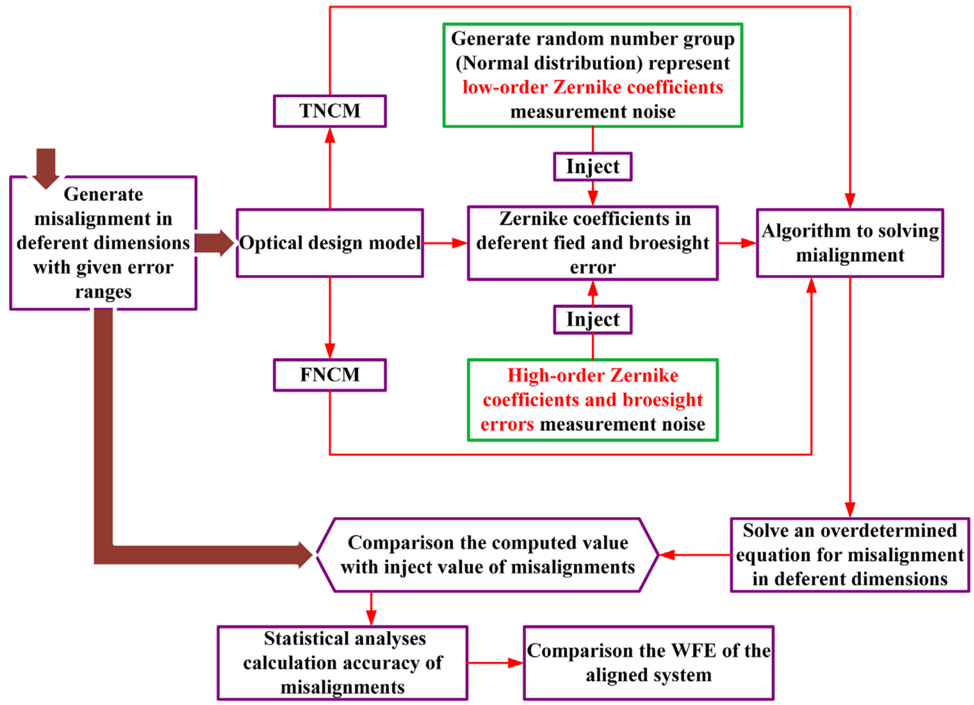

Fig. 6 The comparison verification experiments process.

$$RMSD = \sqrt{\frac{1}{n}\sum_{i=1}^{n}[X(i)_{true} - X(i)_{calculated}]^2}, \tag{31}$$

where $X(i)_{true}$ represents the misalignment introduced, $X(i)_{calculated}$ represents the misalignment calculated, and $n = 500$, which represents the number of misaligned samples. The calculation results are shown in Table 4.

Table 4 could further verify the result of the calculated misalignments in Figs. 7–9. For different misalignment error ranges, the RMSD of each misalignment degree of freedom of the SM and the TM are basically maintained at the same order of magnitude. This shows that the size of the misalignment error ranges has little effect on the result of the system alignment.

To confirm the alignment result of the proposed TNCM from the perspective of system wavefront errors (WFE) correction, the average RMS WFE of the full FOV before and after alignment by FNCM and TNCM, respectively, is calculated, and its schematic diagram is shown in Fig. 10.

It can be observed from Fig. 10 that for three different misalignment error ranges, TNCM has obtained an ideal correction effect, and the average RMS WFE of the full FOV can be all corrected to below 0.0574 waves. At the same time, the comparative experiment results show that FNCM can also obtain a correction effect similar to that of TNCM without considering the measurement noise.

5.2 *Simulation Alignment with Measurement Noise*

In the process of actual laboratorial alignment procedure, there will be environmental factors such as vibration and unstable airflow that affect the measurement accuracy of Zernike coefficients and boresight errors, thus negatively affecting the calculation accuracy and robustness of TNCM and FNCM. To simulate the random noise generated by the actual situation, noise amount $\omega_{normrnd}(\mu = 0, \sigma)$ was added to Zernike coefficients and boresight errors ($\Delta\vec{H}$), as shown in Eqs. (32) and (33). $\omega_{normrnd}(\mu = 0, \sigma)$ is a random number with a mean value of μ and a standard deviation of σ, which obeys normal distribution. In the simulated noise test, the physical significance of σ indicates the magnitude of the noise.

$$[C_i]_{TNCM} = [C_{5-9}] + \omega_{normrnd}(\mu = 0, \sigma), \tag{32}$$

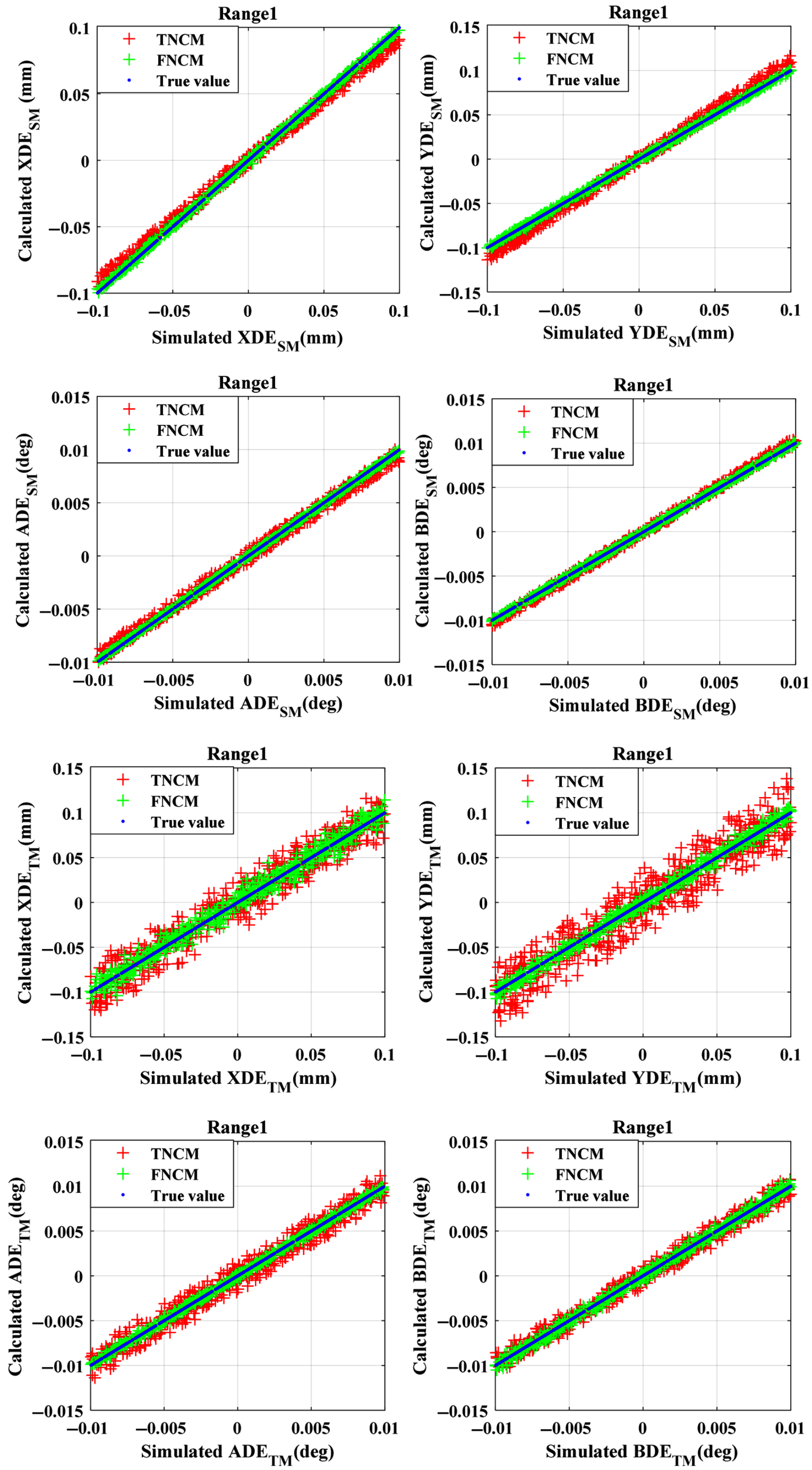

Fig. 7 A comparison between the simulated misalignments and calculated misalignments of the SM and TM of the system, with the misalignment error range as Range1. It is worth noting that the red spot represents the calculated value of TNCM, the green spot represents the calculated value of FNCM, and the blue spot represents the true value.

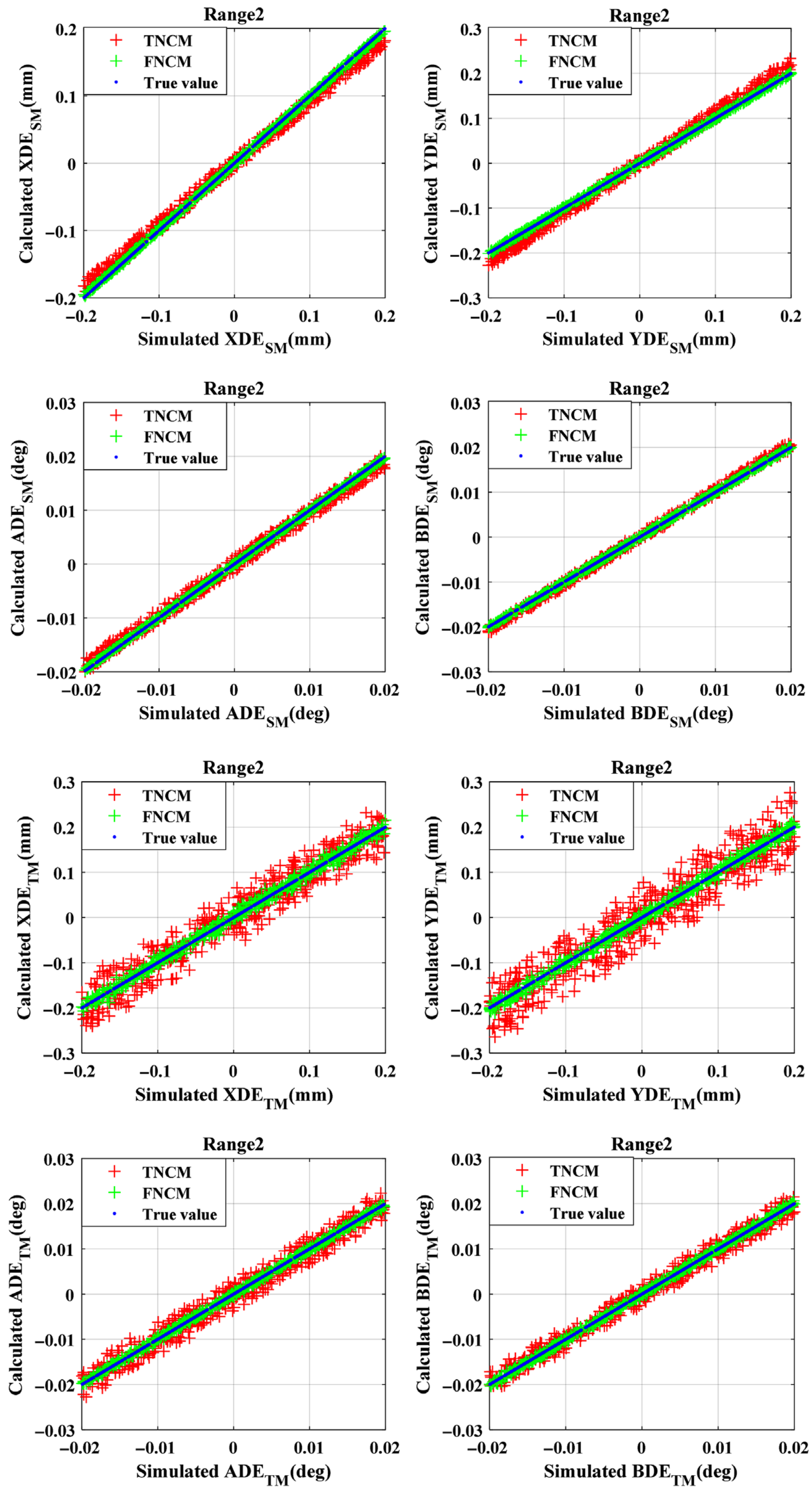

Fig. 8 A comparison between the simulated misalignments and calculated misalignments of the SM and TM of the system, with the misalignment error range as Range 2. It is worth noting that the red spot represents the calculated value of TNCM, the green spot represents the calculated value of FNCM, and the blue spot represents the true values.

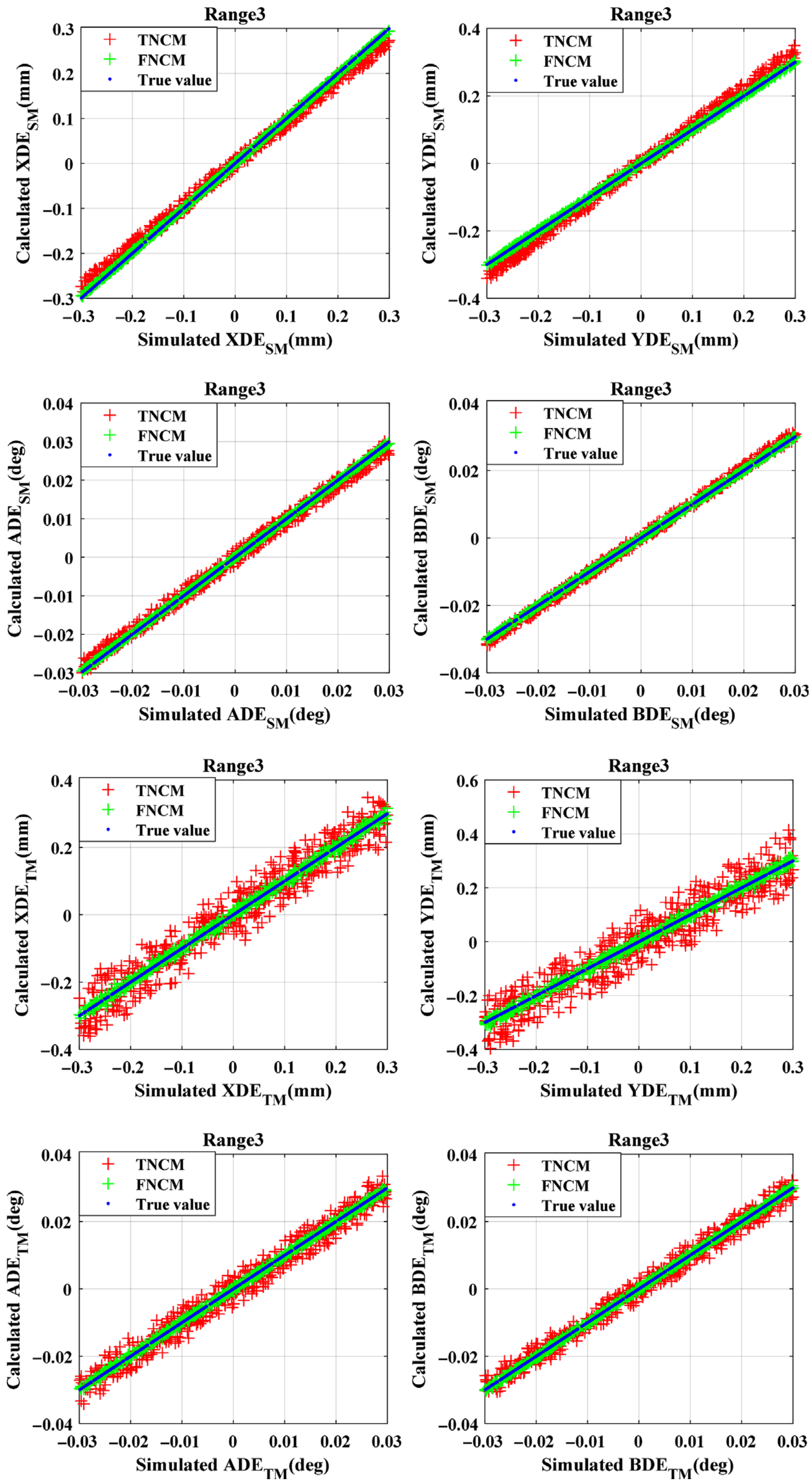

Fig. 9 A comparison between the simulated misalignments and calculated misalignments. between of the SM and TM of the system, with the misalignment error range as Range3. It is worth noting that the red spot represents the calculated value of TNCM, the green spot represents the calculated value of FNCM, and the blue spot represents the true value.

Table 4 The RMSD between the simulated misalignments and the calculated misalignments.

	TNCM			FNCM		
	Range 1	Range 2	Range 3	Range 1	Range 2	Range 3
XDE_{SM}	5.360×10^{-3}	1.079×10^{-2}	1.620×10^{-2}	1.425×10^{-3}	2.030×10^{-3}	2.747×10^{-3}
YDE_{SM}	7.297×10^{-3}	1.455×10^{-2}	2.184×10^{-2}	1.300×10^{-3}	1.923×10^{-3}	2.675×10^{-3}
ADE_{SM}	4.792×10^{-4}	9.486×10^{-4}	1.423×10^{-3}	9.033×10^{-5}	1.352×10^{-4}	1.909×10^{-4}
BDE_{SM}	3.241×10^{-4}	6.681×10^{-4}	1.002×10^{-3}	8.340×10^{-5}	1.185×10^{-4}	1.573×10^{-4}
XDE_{TM}	1.334×10^{-2}	2.760×10^{-2}	4.140×10^{-2}	6.827×10^{-3}	7.159×10^{-3}	7.529×10^{-3}
YDE_{TM}	1.838×10^{-2}	3.624×10^{-2}	5.436×10^{-2}	4.682×10^{-3}	6.790×10^{-3}	9.478×10^{-3}
ADE_{TM}	8.656×10^{-4}	1.710×10^{-3}	2.565×10^{-3}	2.219×10^{-4}	3.281×10^{-4}	4.601×10^{-4}
BDE_{TM}	6.308×10^{-4}	1.298×10^{-3}	1.947×10^{-3}	3.210×10^{-4}	3.360×10^{-4}	3.530×10^{-4}

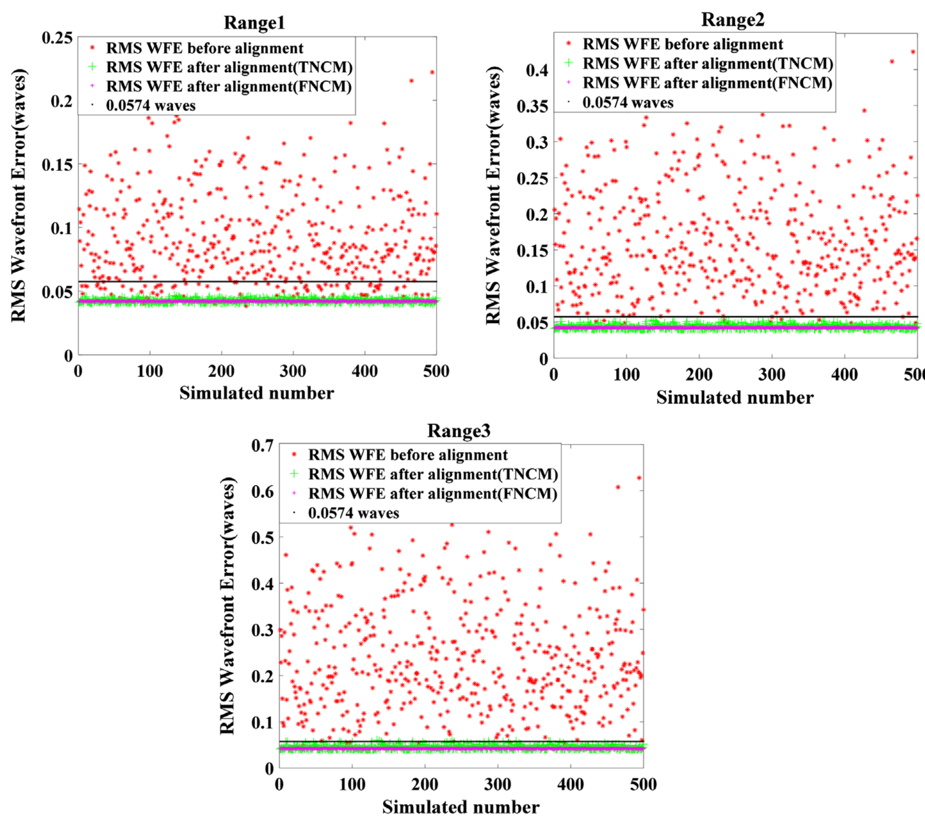

Fig. 10 Average RMS WFE of the full FOV before and after alignment for different error ranges. It is worth noting that the red spot represents the RMS WFE before alignment. The green spot represents the RMS WFE after alignment of TNCM. The purple spot represents the RMS WFE after alignment of FNCM. The black spot represents the maximum RMS WFE of the full FOV in nominal design (0.0574 waves).

$$\begin{cases} [C_i]_{FNCM} = [C_{5-16}] + \omega_{normrnd}(\mu = 0, \sigma) \\ \Delta\vec{H}_{FNCM} = \begin{bmatrix} \Delta\vec{H}_x \\ \Delta\vec{H}_y \end{bmatrix} + \begin{bmatrix} \omega_{normrnd}(\mu = 0, \sigma) \\ \omega_{normrnd}(\mu = 0, \sigma) \end{bmatrix} \end{cases}. \tag{33}$$

In the experiments, the noise is divided into three grades according to the actual measured laboratory noise level data and the spatial scale of the optical system, as shown in Table 5. Each

Table 5 Three types of noise grades.

	Zernike coefficient (λ)	Boresight error (μm)
Grade 1	0.02	3
Grade 2	0.05	5
Grade 3	0.08	8

noise grade contains 500 random noise experiments. TNCM and FNCM are used to perform Monte-Carlo simulation alignment experiments on the misaligned system. The simulation alignment experiments are carried out with the misalignment error range as Range 3. The calculation results of each dimension of misalignment of TNCM and FNCM under different noise grades are shown in Figs. 11, 12, 13, and Table 6.

The simulation experiment results in Figs. 11, 12, 13, and Table 6 show that each misalignment of TNCM can still obtain converging calculation results under different noise grades. The calculation accuracy of XDE and YDE is basically maintained at the order of 10^{-2} under different noise grades, ADE and BDE is basically maintained at the order of 10^{-3} under different noise grades. However, the calculation accuracy of each misalignment of FNCM is significantly reduced after adding noise, and even in the cases of Grade 2 and Grade 3, the calculation accuracy of misalignments is $>10^{-1}$.

To further investigate the alignment accuracy of different models on system wave aberration, the root-mean-square deviation of the average RMS WFE is introduced, which is defined as the following equation.

$$RMSD_{WFE} = \sqrt{\frac{1}{n}\sum_{i=1}^{n}[(WFE^{\text{Average}})_i^{aligne} - (WFE^{\text{Average}})_i^{design}]^2}, \tag{34}$$

In the above equation, n is the number of misalignment samples ($n = 500$). $(WFE^{\text{Average}})_i^{aligne}$ is the average RMS WFE after alignment for misalignment sample i, $(WFE^{\text{Average}})_i^{design}$ represents the average RMS WFE in nominal design. The results are as follows.

Table 7 shows the $RMSD_{WFE}$ of TNCM and FNCM with different noise grades, and Fig. 14 shows the average RMS WFE before and after alignment with different noise grades. The relationship between the $RMSD_{WFE}$ and different noise grades is shown in Fig. 15.

It can be seen from Figs. 14, 15, and Table 7 that the alignment results of TNCM at different noise grades all meet the requirements of the optical system alignment. The average RMS WFE of the full FOV is all corrected to around 0.0574 waves. The alignment accuracy of the average RMS WFE did not change significantly, and the $RMSD_{WFE}$ basically remained at the order of 10^{-2} waves. In addition, the $RMSD_{WFE}$ of 500 experimental samples increased with the increase of noise grades, and they exhibit a roughly linear relationship. This shows that the effect of the alignment of TNCM becomes worse with the increase of noise grades. Therefore, it is still necessary to control the noise level in a reasonable range in actual alignment experiments. However, FNCM fails to meet the requirements of the optical system alignment under different noise grades. In Grade 2 and Grade 3, the optical system completely fails to be aligned.

The above simulation experiments use 5 FOVs to calculate misalignments [F0, F2, F4, F6, F8 in Fig. 3(a)]. To verify the influence of the number of FOVs on the alignment accuracy and alignment effect of TNCM and FNCM, the following two FOVs, three FOVs, seven FOVs, and nine FOVs will be respectively adopted to carry out Monte-Carlo simulation experiments, with the misalignment error range as Range 3. The combinations of FOVs are shown in Table 8.

The simulation results are as follows, Table 9 shows the $RMSD_{WFE}$ for different noise grades and the number of measured FOVs, whereas Fig. 16 shows the relationship between the $RMSD_{WFE}$ and the number of measured FOVs under different noise grades.

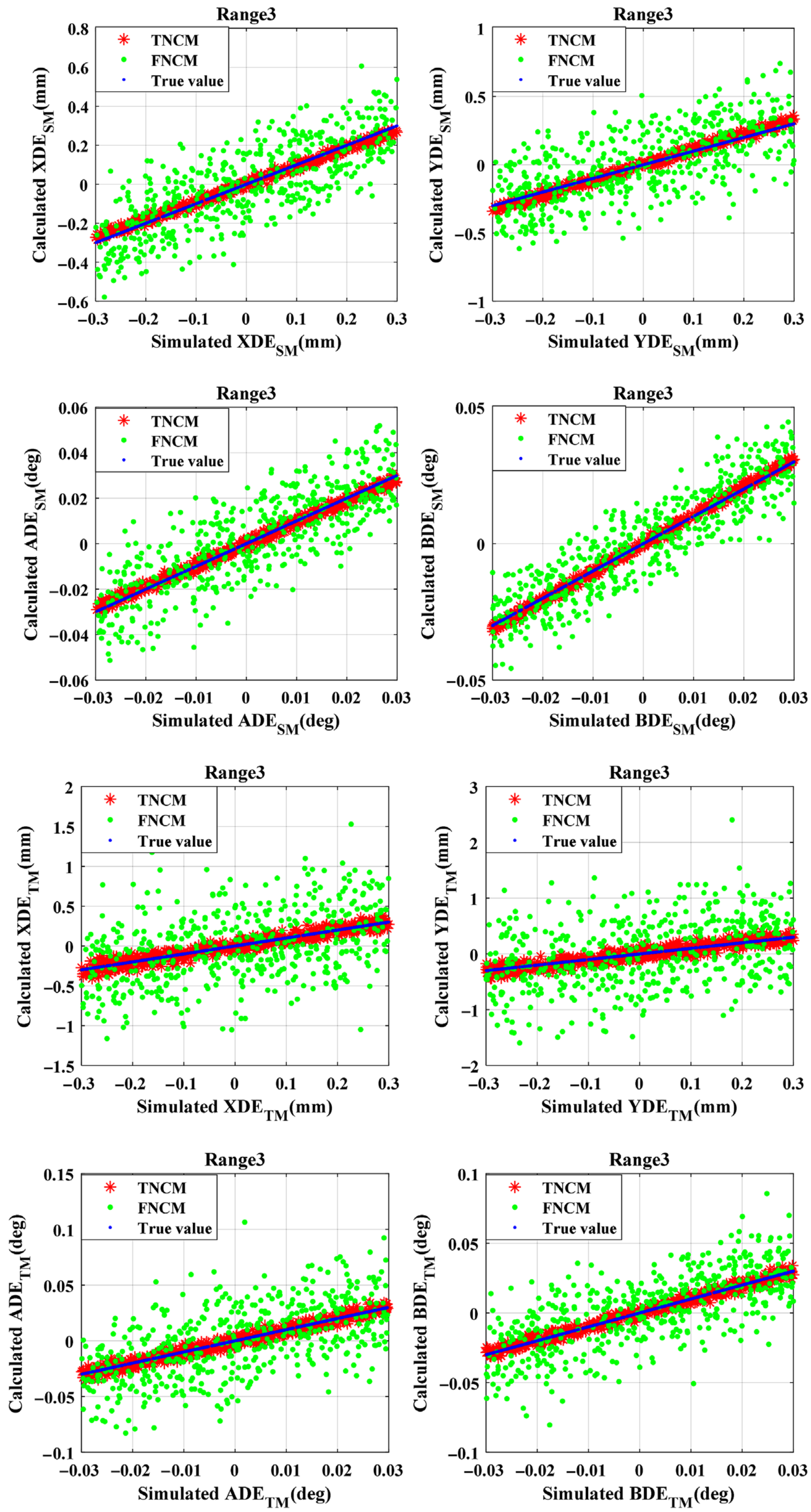

Fig. 11 A comparison between the simulated misalignments and calculated misalignments of the SM and TM of the system, with the noise grade as Grade 1. It is worth noting that the red spot represents the calculated values of TNCM, the green spot represents the calculated values of FNCM, and the blue spot represents the true values.

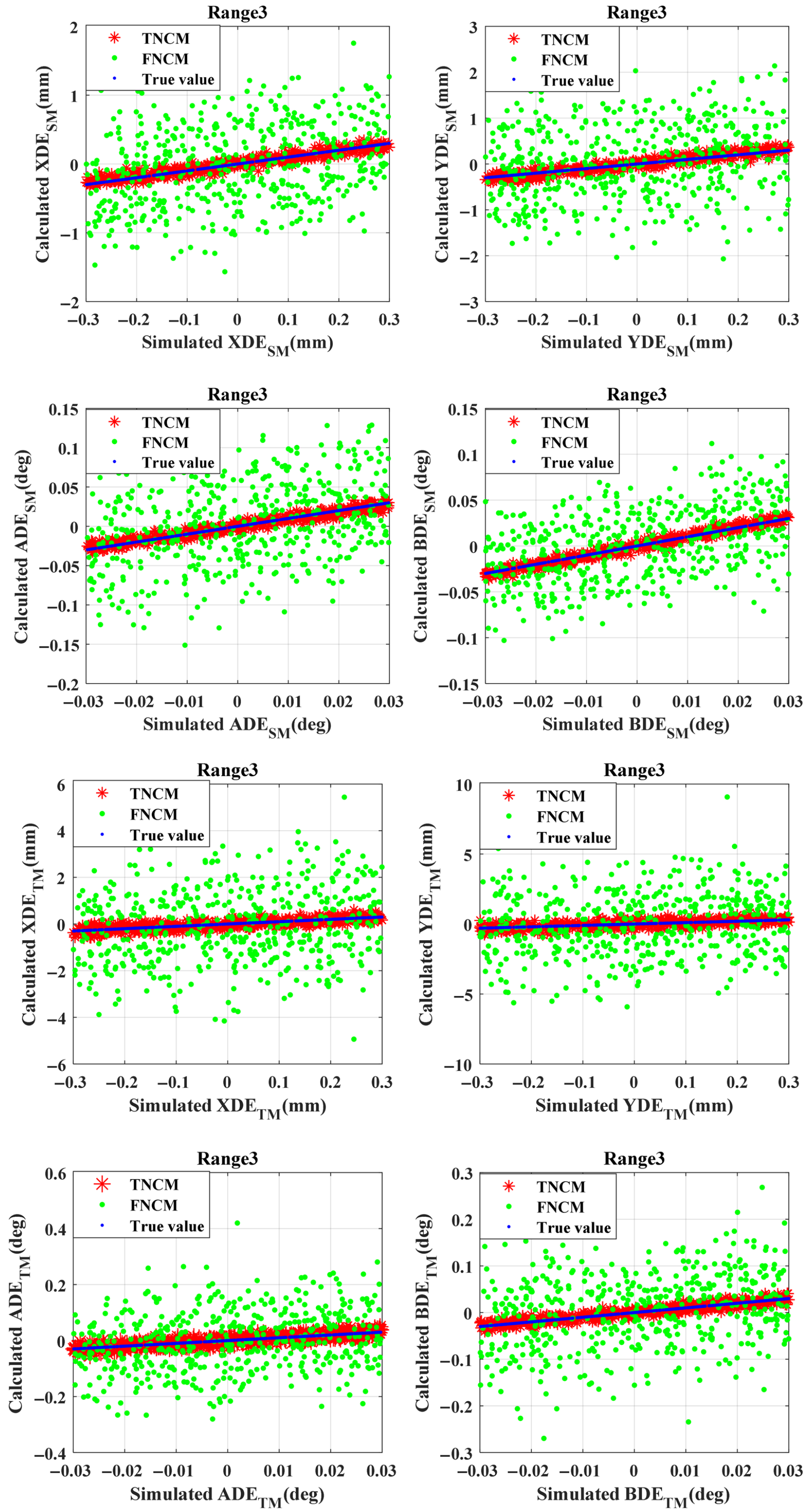

Fig. 12 A comparison between the simulated misalignments and calculated misalignments of the SM and TM of the system, with the noise grade as Grade 2. It is worth noting that the red spot represents the calculated values of TNCM, the green spot represents the calculated value of FNCM, and the blue spot represents the true values.

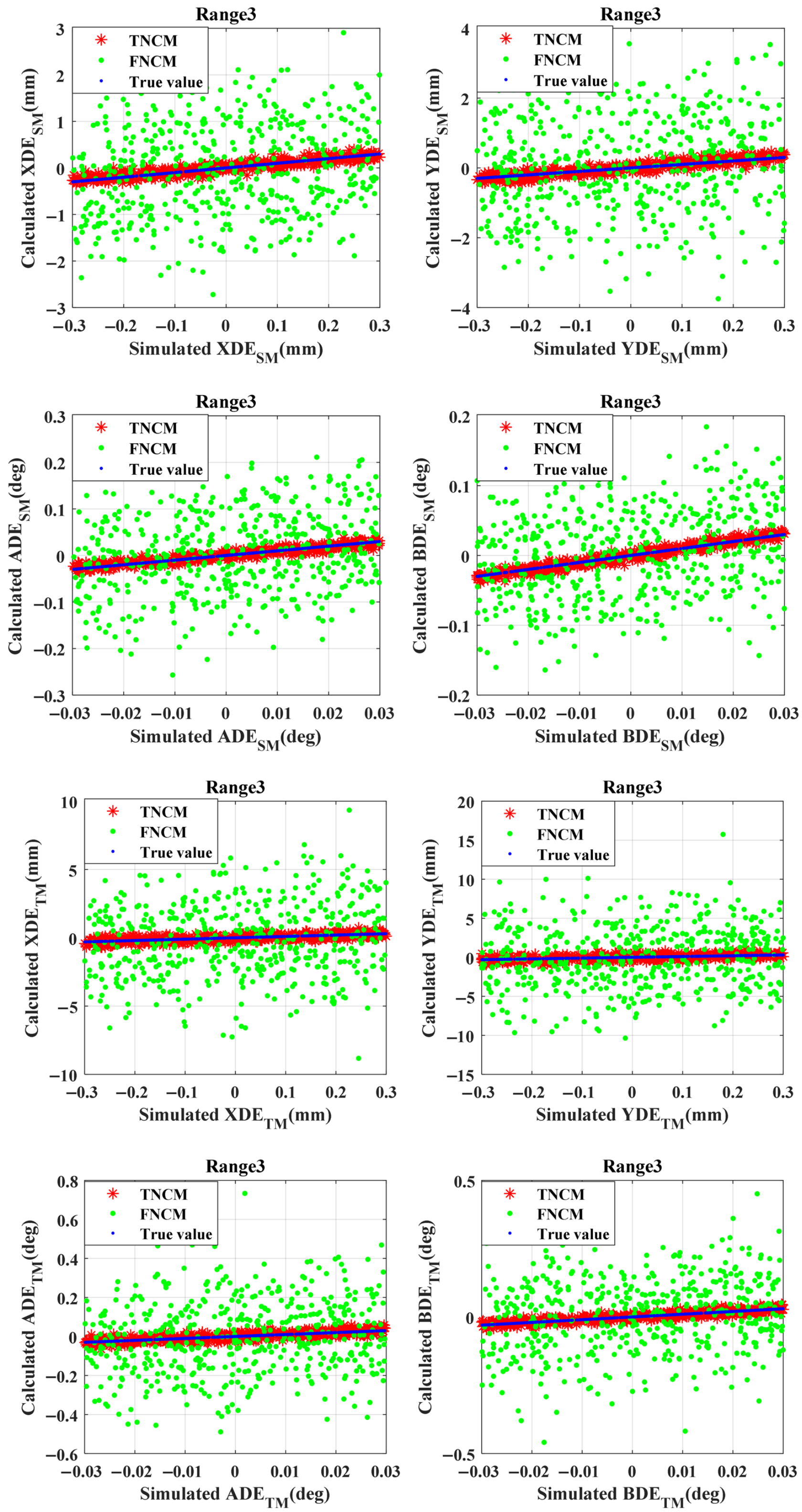

Fig. 13 A comparison between the simulated misalignments and calculated misalignments of the SM and TM of the system, with the noise grade as Grade 3. It is worth noting that the red spot represents the calculated value of TNCM, the green spot represents the calculated value of FNCM, and the blue spot represents the true value.

Table 6 The RMSD in different noise grades.

	TNCM			FNCM		
	Grade 1	Grade 2	Grade 3	Grade 1	Grade 2	Grade 3
XDE_{SM}	1.877×10^{-2}	4.695×10^{-2}	6.345×10^{-2}	1.394×10^{-1}	5.575×10^{-1}	1.012
YDE_{SM}	2.517×10^{-2}	6.189×10^{-2}	8.349×10^{-2}	1.972×10^{-1}	7.891×10^{-1}	1.282
ADE_{SM}	1.627×10^{-3}	3.912×10^{-3}	5.267×10^{-3}	1.240×10^{-2}	4.963×10^{-2}	8.065×10^{-2}
BDE_{SM}	1.166×10^{-3}	2.946×10^{-3}	3.985×10^{-3}	8.769×10^{-3}	3.506×10^{-2}	5.698×10^{-2}
XDE_{TM}	4.889×10^{-2}	1.284×10^{-1}	1.743×10^{-1}	4.067×10^{-1}	1.626	2.642
YDE_{TM}	6.756×10^{-2}	1.994×10^{-1}	2.731×10^{-1}	5.642×10^{-1}	2.258	3.669
ADE_{TM}	3.183×10^{-3}	9.373×10^{-3}	1.283×10^{-2}	2.651×10^{-2}	1.060×10^{-1}	1.724×10^{-1}
BDE_{TM}	2.298×10^{-3}	6.035×10^{-3}	8.191×10^{-3}	1.911×10^{-2}	7.640×10^{-2}	1.241×10^{-1}

Table 7 The $RMSD_{WFE}$ in different noise grades.

	Without noise	Grade1	Grade2	Grade3
TNCM	6.504×10^{-3}	7.351×10^{-3}	2.234×10^{-2}	3.342×10^{-2}
FNCM	2.260×10^{-3}	9.904×10^{-2}	4.784×10^{-1}	8.619×10^{-1}

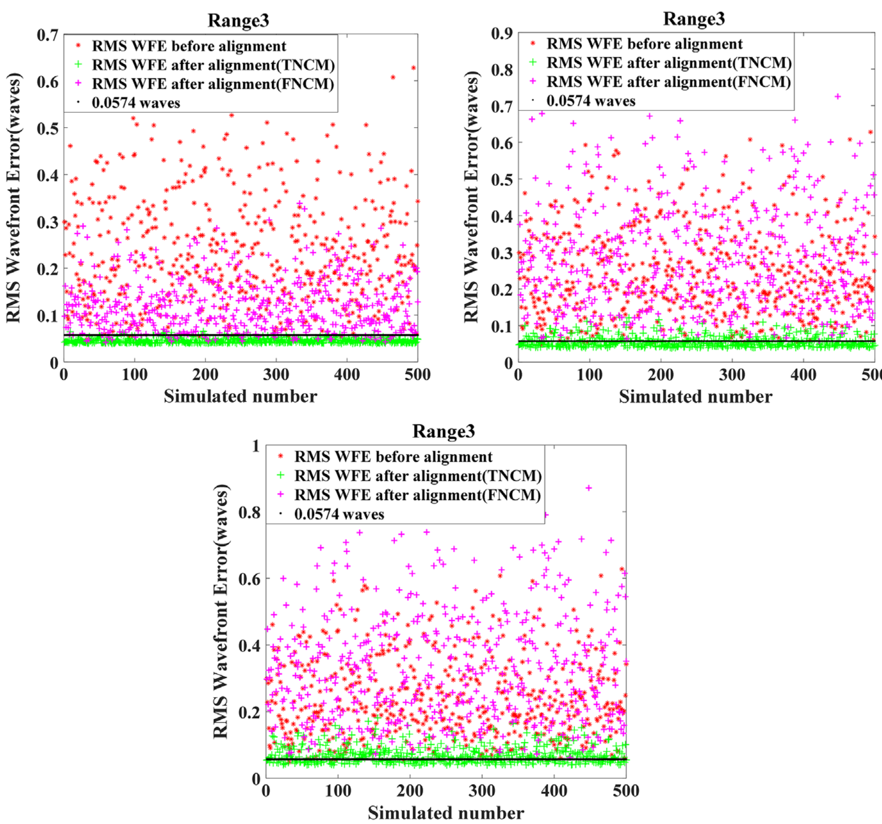

Fig. 14 Average RMS WFE of the full FOV before and after alignment for different noise grades. It is worth noting that the red spot represents the RMS WFE before alignment. The green spot represents the RMS WFE after alignment of TNCM. The purple spot represents the RMS WFE after alignment of FNCM. The black spot represents the maximum RMS WFE of the full FOV in nominal design (0.0574 waves).

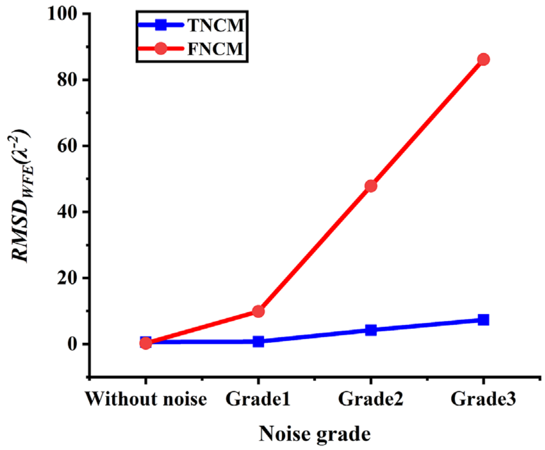

Fig. 15 The relationship between the $RMSD_{WFE}$ and the noise grades under different models.

Table 8 The combinations of FOVs.

Two FOVs	Three FOVs	Seven FOVs	Nine FOVs
F0, F2	F0, F2, F4	F0, F1, F2, F4, F5, F6, F8	F0, F1, F2, F3, F4, F5, F6, F7, F8, F9

Table 9 The $RMSD_{WFE}$ for different noise grades and the number of FOVs.

	Without noise	Grade1	Grade2	Grade3
TNCM				
Two FOVs	6.949×10^{-3}	7.967×10^{-3}	3.956×10^{-2}	6.522×10^{-2}
Three FOVs	6.451×10^{-3}	7.453×10^{-3}	3.028×10^{-2}	4.858×10^{-2}
Seven FOVs	6.397×10^{-3}	7.005×10^{-3}	2.203×10^{-2}	3.189×10^{-2}
Nine FOVs	6.286×10^{-3}	6.862×10^{-3}	2.096×10^{-2}	3.164×10^{-2}
FNCM				
Two FOVs	3.972×10^{-3}	1.374×10^{-1}	5.806×10^{-1}	9.543×10^{-1}
Three FOVs	3.531×10^{-3}	1.108×10^{-1}	4.932×10^{-1}	9.007×10^{-1}
Seven FOVs	2.310×10^{-3}	9.904×10^{-2}	4.579×10^{-1}	8.607×10^{-1}
Nine FOVs	2.191×10^{-3}	1.003×10^{-1}	4.566×10^{-1}	8.647×10^{-1}

It can be seen from Table 9 and Fig. 16 that for TNCM, under noise Grade 1, the alignment result of TNCM is close to that without noise, and the $RMSD_{WFE}$ are basically maintained at the order of 10^{-3}. With the increase of FOVs from 2 to 9, the $RMSD_{WFE}$ changed relatively little as it decreased by 12.6%. This shows that increasing the number of FOVs when the noise level is low cannot effectively suppress the noise. Under Grade 2 and Grade 3, the $RMSD_{WFE}$ is basically maintained at the order of 10^{-2}. With the increase of FOVs from 2 to 5, the $RMSD_{WFE}$ changed significantly as it decreased by 43.5% and 48.8%, respectively. With the increase of FOVs from 5 to 9, however, the $RMSD_{WFE}$ changed relatively little as it decreased by 6.2% and 5.3%, respectively. This shows that when the noise level is relatively large, noise can be

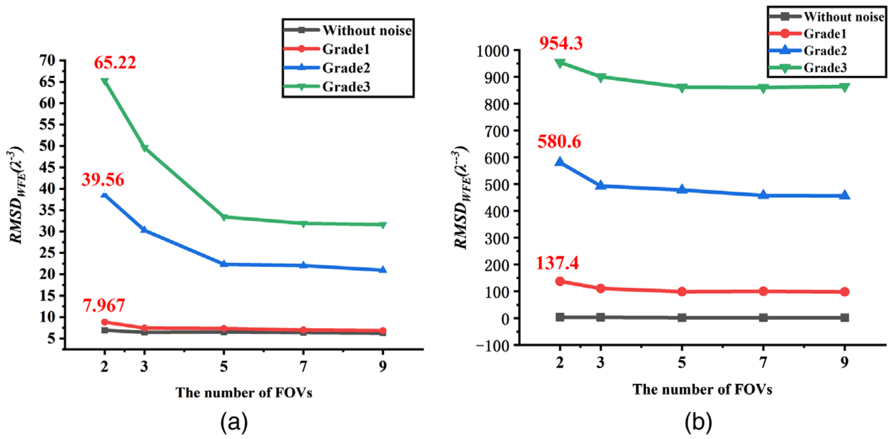

Fig. 16 The relationship between the $RMSD_{WFE}$ and the number of FOVs under different noise grades. (a) TNCM. (b) FNCM. It is worth noting that the black line represents without measurement noise. The red line represents the noise Grade 1.The blue line represents the noise Grade 2. The green line represents the noise Grade 3.

effectively suppressed by increasing the number of measured FOVs, and the robustness of TNCM can thus be enhanced. However, noise cannot be unconditionally suppressed by increasing the number of measured FOVs. In contrast, for FNCM, under different noise grades, with the increase of the number of FOVs, the $RMSD_{WFE}$ is basically maintained at the order of 10^{-1}. This shows that the increase of the number of FOVs cannot effectively improve the robustness of FNCM.

6 Analysis and Discussion

First, TNCM based on quadratic aberration field decenter vectors and FNCM based on high-order Zernike coefficients, and boresight errors can both obtain ideal alignment results, when the measurement noise is not considered. However, through verification experiments, it is discovered that the calculation accuracy of each misalignment dimension of FNCM is slightly higher than that of TNCM. The main reason for this phenomenon could be that during the construction of TNCM, only low-order aberrations were considered to avoid the measurement of higher-order Zernike coefficients, and higher-order aberrations that were not considered had also contributed to the third-order astigmatism field and the third-order coma field of the misaligned off-axis TMA system. However, this has no effect on the alignment of the optical system WFE.

Second, it is found through verification experiments that when the measurement noise is added, the robustness of TNCM is much better than that of FNCM. The main reasons for this phenomenon could be that FNCM constructed using higher-order Zernike coefficients assumes that the WFE of the system and aberration field decenter vectors are linear functions. However, for the misaligned off-axis TMA system with designed tilts and decenters, high-order Zernike coefficients introduced by FNCM have a higher sensitivity to aberration field decenter vectors, which implies poor robustness. In other words, the measurement accuracy of higher-order coefficients has a significant effect on the calculation accuracy of aberration decenter vectors. Therefore, the introduction of high-order Zernike coefficients measurement noise affects the accuracy and convergence of the misalignment calculation. TNCM constructed using the quadratic aberration field decenter vectors only needs to measure third-order Zernike coefficients, which are less sensitive to aberration field decenter vectors. Therefore, TNCM achieves high robustness.

7 Conclusion

In this paper, a misalignment calculation algorithm based on quadratic aberration field decenter vectors is investigated for a misaligned off-axis TMA optical system with designed tilts and decenters. First, two new concepts are introduced: the inherent aberration field decenter vector and the misalignment aberration field decenter vector. Then, the analytical expressions for aberration field decenter vectors of the system are derived. Based on an over-determined system of 8-element quadratic equations, a mathematical and physical model reflecting the mapping relationship between misalignment and the system aberrations is derived and established. Finally, the Monte-Carlo comparison experiments are conducted between the proposed algorithm and the existing fifth-order algorithm.

In the verification experiments without measurement noise, both the proposed TNCM and the existing FNCM can obtain the convergent calculation results, and the RMSD of each misalignment degree of freedom basically reaches below the order of 10^{-3}. Moreover, both algorithms can correct the average RMS WFE of the off-axis TMA optical system to less than 0.0574 waves. Therefore, the correctness of TNCM is verified.

To confirm the practicability of TNCM in the actual alignment process, the robustness of the algorithm was verified by experiments with measurement noise added. The experiment results show that TNCM displays a remarkable advantage over FNCM. For different measurement noise grades, the calculation accuracy of TNCM is higher than that of FNCM. The RMSD of each misalignment degree of freedom is basically below the order of 10^{-2}, and the average RMS WFE of the optical system can all be corrected to about 0.0574 waves. In contrast, the robustness of FNCM is significantly affected by noise, and the optical system alignment even failed completely under noise Grade 2 and noise Grade 3. In addition, the experiments show that increasing the number of measurement FOVs when the noise level is low cannot effectively suppress the noise. Yet when the noise level is large, the noise can be effectively suppressed by increasing the number of measured FOVs.

Research results show that the established TNCM based on quadratic aberration field decenter vectors shows better robustness. In actual alignment experiments of off-axis TMA space telescopes, this algorithm only requires one to measure the low-order Zernike coefficients of different FOVs. Therefore, this algorithm effectively avoids large measurement error of high-order Zernike coefficients and difficult measurement of boresight errors and simplifies the control requirements for alignment environments.

Acknowledgments

This research was supported by the National Natural Science Foundation of China (NSFC) (Grant Nos. 61875190 and 12003033). Disclosures: The authors declare no conflicts of interest.

References

1. H. J. Juranek et al., “Off-axis telescopes: the future generation of Earth observation telescopes,” *Proc. SPIE* **3439**, 104–115 (1998)
2. J. Sasián et al., “Active reconstruction and alignment strategies for the advanced technology solar telescope,” *Proc. SPIE* **7793**, 77930E (2010).
3. L. M. Stepp et al., “Active optics in large synoptic survey telescope,” *Proc. SPIE* **8444**, 84444Q (2012).
4. D. Scott Acton et al., “Wavefront sensing and controls for the James Webb Space Telescope,” *Proc. SPIE* **8442**, 84422H (2012).
5. R. Holzlöhner et al., “Fast active optics control of wide-field telescopes based on science image analysis,” *Proc. SPIE* **9151**, 91512I (2014).
6. G. Ju et al., “Analytic approach for segment-level wavefront sensing in the global alignment progress based on image feature analysis,” *J. Astron. Telesc. Instrum. Syst.* **6**(2), 029003 (2020).
7. H. P. Stahl, M. Postman, and W. R. Arnold Sr., “ATLAST-8 Mission concept study for 8-meter Monolithic UV/Optical Space Telescope,” *Proc. SPIE* **7731**, 77312N (2010).
8. J. R. Kuhn and S. L. Hawley, “Some astronomical performance advantages of off-axis telescopes,” *Publ. Astron. Soc. Pac.* **111** (759), 601–620 (1999)

9. K. P. Thompson et al., "Validation of the corrective optics on the Hubble Space Telescope 1st Servicing Mission," *J. Astron. Telesc. Instrum. Syst.* **2**(3), 034001 (2016).
10. M. Clampin, "Status of the James Webb space telescope observatory," *Proc. SPIE* **8442**, 84422A (2012).
11. X.-T. Zhao et al., "Study on computer-aided alignment method of a three-mirror off-axis aspherical optical system," *Proc. SPIE* **7656**, 76566M (2010).
12. F. Zeng et al., "Optics ellipticity performance of an unobscured off-axis space telescope," *Opt. Express* **22**(21), 25277–25285 (2014).
13. Z. Gu, Y. Wang, and G. Ju, "Computation of misalignment and primary mirror astigmatism figure error of two-mirror telescopes," *J. Astron. Telesc. Instrum. Syst.* **4**(1), 019002 (2018).
14. J. M. Sasian et al., "Misalignment parameters estimation in refractive optical systems," *Proc. SPIE* **7068**, 70680P (2008).
15. R. Upton, T. Rimmele, and R. Hubbard, "Active optical alignment of the Advanced Technology Solar Telescope," *Proc. SPIE* **6271**, 62710R (2006).
16. M. A. Lundgren and W. L. Wolfe, "Alignment of a three-mirror off-axis telescope by reverse optimization," *Opt. Eng.* **30**(3), 307–311 (1991)
17. H. Lee et al., "Computer-guided alignment II :optical system alignment using differential wavefront sampling," *Opt. Express* **15**(23), 15424–15437 (2007)
18. R. V. Shack and K. P. Thompson, "Influence of alignment errors of a telescope system," *Proc. SPIE* **0251**, 146–153 (1980).
19. K. P. Thompson, "Aberration fields in tilted and decentered optical systems," Ph.D. dissertation, University of Arizona (1980).
20. K. P. Thompson, "Description of the third-order optical aberrations of near-circular pupil optical systems without symmetry," *J. Opt. Soc. Am. A* **22**(7), 1389–1401 (2005)
21. K. P. Thompson, "Multinodal fifth-order optical aberrations of optical systems without rotational symmetry: spherical aberration," *J. Opt. Soc. Am. A* **26**(5), 1090–1100 (2009).
22. K. P. Thompson, "Multinodal fifth-order optical aberrations of optical systems without rotational symmetry: the comatic aberrations," *J. Opt. Soc. Am. A* **27**(6), 1490–1504 (2010).
23. K. P. Thompson, "Multinodal fifth-order optical aberrations of optical systems without rotational symmetry: the astigmatic aberrations," *J. Opt. Soc. Am. A* **28**(5), 821–836 (2011).
24. H. H. Hopkins, *The Wave Theory of Aberrations*, Oxford (1950).
25. R. A. Buchroeder, "Tilted component optical systems," Ph.D. dissertation, University of Arizona, Arizona (1976).
26. T. Schmid, K. P. Thompson, and J. P. Rolland, "Misalignment-induced nodal aberration fields in two-mirror astronomical telescopes," *Appl. Opt.* **49**(16), D131–D144 (2010)
27. K. P. Thompson, T. Schmid, and J. P. Rolland, "The misalignment induced aberrations of TMA telescopes," *Opt. Express* **16**(25), 20345–20353 (2008)
28. G. Ju et al., "Experimental study on the extension of nodal aberration theory to pupil-offset off-axis three-mirror anastigmatic telescopes," *J. Astron. Telesc. Instrum. Syst.* **5**(2), 029001 (2019).
29. J. Sebag et al., "LSST telescope alignment plan based on nodal aberration theory," *Publ. Astron. Soc. Pac.* **124**(914), 380–390 (2012).
30. Z. Gu, C. Yan, and Y. Wang, "Alignment of a three-mirror anastigmatic telescope using nodal aberration theory," *Opt. Express* **23**(19), 25182–25201 (2015).
31. X. Zhang et al., "Active optical alignment of off-axis telescopes based on nodal aberration theory," *Opt. Express* **24**(23), 26392–26413 (2016).
32. K. P. Thompson et al., "Real-ray-based method for locating individual surface aberration field centers in imaging optical systems without rotational symmetry," *J. Opt. Soc. Am. A* **26**(6), 1503–1517 (2009).
33. E. D. Kim et al., "Reverse-optimization alignment algorithm using Zernike sensitivity," *J. Opt. Soc. Korea* **9**(2), 68–73 (2005).
34. R. W. Gray and J. P. Rolland, "Wavefront aberration function in terms of R. V. Shack's vector product and Zernike polynomial vectors," *J. Opt. Soc. Am. A* **32**(10), 1836–1847 (2015).

Jinxin Wang is currently studying for an optical engineering doctoral degree at Changchun Institute of Optics, Fine Mechanics and Physics, Chinese Academy of Science. His research interests include CAA algorithms for large-aperture space telescopes, aberration theories, and unconventional optical system design.

Xu He is a professor at CIOMP who specializes in the fabrication of space-based large aperture segmented telescopes, aberration theories, and optical alignment.

Xiaohui Zhang is a professor at CIOMP. Her research interests include space optical remote sensing technology, multispectral, and hyperspectral remote sensing imaging technology.

Jing Luo is a researcher at CIOMP who specializes in optical measurements and optical simulations.